Quantitative facies analysis of a fluvio-aeolian system: Lower Triassic Buntsandstein Group, eastern France

Lucas Bofill, Guilherme Bozetti, Gerhard Schäfer, Jean-François Ghienne, Mathieu Schuster, Claiton Scherer, Ezequiel de Souza

Quantitative facies analysis of a fluvio-aeolian system: Lower Triassic Buntsandstein Group, eastern France

Lucas Bofill[1*], Guilherme Bozetti[1], Gerhard Schäfer[1], Jean-François Ghienne[1], Mathieu Schuster[1], Claiton Scherer [2], Ezequiel de Souza [3]

[1] Institut Terre et Environnement de Strasbourg (UMR7063), CNRS, Université de Strasbourg,France
[2] Instituto de Geociências, Universidade Federal do Rio Grande do Sul, Porto Alegre, 90650 001, Brazil
[3] Universidade Federal do PAMPA, Caçapava do Sul, Brazil
* Corresponding author: lucasbofill@yahoo.com.br

ABSTRACT

Understanding the factors that control the temporal and spatial evolution of the Lower Triassic Buntsandstein Group, eastern France, is important not just for palaeoenvironmental reconstruction but also because it is an important reservoir for the lithium-rich geothermal brines in the Upper Rhine Graben region. The interval of interest in this study, the Lower Grès Vosgien Formation (LGV), is made up of c. 200 metres of clastic deposits of mixed fluvial and aeolian origin. Given the proximity between the outcrops and the areas of mineral and heat exploration, this region offers a unique opportunity for quantitative analysis and correlation between outcrops and reservoir. The LGV is the thickest Formation in the Buntsandstein Group. However, hitherto, no detailed architectural analysis has been published to reveal the controlling factors of its depositional elements. In this study, high-resolution facies analysis was applied to thirteen outcrops, and a core, to quantify fluvial and aeolian depositional architectures, and to comprehend palaeoenvironmental conditions during their deposition. Two facies associations were identified. The fluvial channel facies association, composed mainly of sandstones deposited in poorly confined, occasionally ephemeral channels, corresponds to 93% of the total thickness. The analysis of more than 800 sets of strata characterised by lower-, transitional-, and upper-flow regime sedimentary structures, distributed within different architectural elements, enabled the distinction of temporal and spatial variabilities, and an estimate of fluvial palaeohydraulic characteristics. The wind- and water-laid facies association, which accounts for 7% of the total thickness, records an architecture controlled by a fluctuating water-table level, and ephemeral floods. Results revealed that aeolian dunes and sand sheets accumulated in distinct temporal moments. The vertical trends, recorded in the core, indicate an upward increase in the frequency of intercalations between the two facies associations, and a decrease in the occurrences of thicker cross-bedded sandstone sets of fluvial origin, which, associated with the overall retrogradational stacking pattern of the LGV, is interpreted as the preserved record of a large distributive fluvial system (DFS). The occurrence of laterally extensive aeolian deposits, overlying fluvial deposits, is often associated by authors with periods of relatively more arid conditions at a regional scale. However, evidence indicates channel belt avulsion as an alternative interpretation for the establishment of the two facies associations. The findings enhance the knowledge about the depositional controlling factors in braided fluvial and aeolian

systems, and improves predictive models that account for reservoir heterogeneity in accumulated successions of this type.

Keywords: Braided fluvial, aeolian, Lower Triassic, Buntsandstein, quantitative facies analysis.

1. INTRODUCTION

The major role of continental depositional systems as subsurface sedimentary reservoirs, which may act as hosts for georesources, and the significance of facies scale heterogeneities in fluid-flow behaviour (Høimyr et al., 1992), justify the prolonged history of studies on the factors that control deposition in continental environments (e.g. Miall, 1977; Røe, 1987; Kocurek, 1988; Langford, 1989; Havholm and Kocurek, 1994; Hjellbakk, 1997; Mountney et al., 1999; Scherer and Lavina, 2005; Fielding, 2006; Weissmann et al., 2010; Wang and Plink-Björklund, 2019; Ventra and Moscariello, 2023). The quantitative analysis of sedimentary deposits is crucial for understanding depositional processes and palaeoenvironmental conditions (e.g. Leclair and Bridge, 2001; Hansford and Plink-Björklund, 2020; Hartley and Owen, 2022; Reis et al., 2022; McLeod et al., 2023; Colombera et al., 2024). Likewise, quantitative sedimentary analysis aids in the refinement of landscape evolution models, and to improve predictions of subsurface reservoirs (Colombera et al., 2013).

Triassic continental deposits have long served as reservoirs for hydrocarbons and groundwater (e.g. Cowan, 1993; Liu et al., 1996; Rossi et al., 2002; Leleu et al., 2009; McKie, 2011; Medici et al., 2015). This is no different for the Lower Triassic Buntsandstein Group (Gr.) in eastern France (Fig. 1A), which serves as a potable groundwater aquifer (Vaute et al., 2007; 2013), and an established reservoir of lithium- concentrated geothermal brine (Aquilina et al., 1997; Kölbel et al., 2020; Fries et al., 2022; Sanjuan et al., 2022). This succession has also been identified as hosting the most promising lithium reserves in Europe (Sanjuan et al., 2022).

The Lower Grès Vosgien Formation (LGV), Middle Buntsandstein (Olenekian) (Fig. 1B), has been interpreted by Bourquin et al. (2009) to represent the preserved deposits of a braided fluvial system developed upon an arid alluvial plain, and fluvial-aeolian deposits of a marginal erg (aeolian dune field). The authors presented a robust dataset and interpretations of large-scale, vertical and lateral, distribution of the Middle Buntsandstein, undertaking analysis via application of sequence stratigraphic concepts to the continental succession. In this study, a detailed facies architecture characterisation is presented, focused on the LGV, in a scale not targeted by Bourquin et al. (2009).

Preserved intercalation between aeolian and fluvial deposits is often attributed to spatio- temporal alternations between dry and humid climatic phases, respectively (e.g. Clemmensen and Abrahamsen, 1983; Porter, 1987; Havholm and Kocurek, 1994; Jones and Blakey, 1997; Newell, 2001; Farraj and Harvey, 2004; Scherer and Lavina, 2005; Al- Masrahy and Mountney, 2015). The same has been interpreted by Bourquin et al., (2009) for the LGV. Alternatively, it may result from interactions between coexisting aeolian and fluvial processes that influence locally the dynamics of these systems (Jones and Blakey, 1997; Rittner et al., 2016).

Recent advances in interpreting fluvial discharge variability (Plink-Björklund, 2015; Fielding et al., 2018; Sharma et al., 2023; Walker and Holbrook, 2023), palaeohydraulics (Leary and Ganti, 2019; Alexander et al., 2020; Lyster et al., 2022; Ohata et al., 2022; Hartley and Owen, 2022; Colombera et al, 2023), and spatial versus temporal variations in fluvial (Colombera and Mountney, 2019; Herbert et al., 2019; Priddy and Clarke, 2021; Lyster et al., 2022; Walker and Holbrook, 2023), and aeolian (Cosgrove et al., 2021; Gross et al., 2022; Kifumbi et al., 2023) systems, emphasise the need to refine existing facies models of previously studied formations. The aim of this study is to use qualitative and quantitative facies and architectural characterisation, at different scales, to understand the factors that controlled the depositional evolution of the Lower Grès Vosgien Formation. The following research questions are answered: i) What are the proportions of the different elements that compose the LGV? ii) What are the evidence of spatial vs. temporal flow conditions variations, in dryland rivers? iii) How do water-table level fluctuations, and ephemeral floods, control the architecture of aeolian deposits? iv) How do the different facies associations evolve spatially and temporally, and what do they reveal about the large- scale depositional system?

2. STUDY AREA AND GEOLOGICAL SETTING

The study area is situated in eastern France, along the western shoulders of the Upper Rhine Graben (URG), where the Buntsandstein Group (Gr.) crops out at the Vosges mountains, and where the EPS1 well was drilled and cored, at Soultz-sous-Forêts (Fig. 1C) (e.g. Gérard et al., 2006; Kölbel and Genter, 2017). The Buntsandstein Gr. was deposited during the Lower Triassic along the western margin of the German Basin in a sedimentation area extending across eastern France, Switzerland, Luxemburg, Belgium, Netherlands, Germany, Poland and Denmark (Gall et al., 1977). The region experienced predominantly continental sedimentation attributed to braided-river deposition either on crystalline basement or on restricted Late Permian intracontinental basins (Dachroth, 1985; Deynoux et al., 1997; Bourquin et al., 2009). Different geological formations are recognised within the Buntsandstein Gr. depending on the lateral position in the basin (Mader, 1985).

This study targets the thickest unit of the Buntsandstein Gr. in eastern France, known as the Lower Grès Vosgien Formation (LGV) (Théobald et al., 1967) (Fig. 1B), which attains a maximum thickness of ~200 m in the region of Soultz-sous-Forêts (Aichholzer, 2019). The LGV is composed of braided fluvial and aeolian sandstones deposited under arid conditions (Dalchroth, 1985; Bourquin et al., 2006; Bourquin et al., 2009), interfingered with rare centimetre-thick claystone layers of floodplain origin (Ghienne et al., 1994; Bourquin et al., 2006; Bourquin et al., 2009).

During the Late Eocene, the URG was formed in front of the alpine compression, reactivating normal faulting structures from the Variscan orogeny (Grimmer et al., 2017) that resulted in burial of the Triassic Buntsandstein Gr. to depths of approximately 1000 m to 1400 m (Aichholzer, 2019). In contrast to the basin axis, the elevated portions of the URG expose the Buntsandstein Gr. deposits along the Vosges and Black Forest mountains. This geological setting offers an ideal opportunity to study these outcrops as analogues for reservoir characterisation, given the actual reservoir and its analogues belong to the same geological formation, and are situated geographically close to each other (Fig. 1).

3. METHODS AND MATERIALS

Sedimentological data were collected through vertical profile descriptions at scale of 1:50 from thirteen outcrops (Fig. 1C), totalling 290 m of rock succession, and from the upper 100 m of the LGV of the well EPS1. The height of the outcrops varies from 7 m to 40 m. Facies were coded following the principles outlined by Miall (1977), and for facies analysis, the framework of Walker (1992) was adopted, grouping genetically related facies into facies associations. Within the facies associations, specific morphologies were defined as architectural elements (Allen, 1983a; Miall, 1985).

Considering that vertical profiles alone are insufficient for fluvial sedimentology analysis due to the numerous lateral facies changes (Miall, 1988), characterisation of fluvial architectural elements was conducted from seven out of the thirteen outcrops. In outcrop LGV7 (Fig. 1C), a Digital Outcrop Model was used, created with a DJI Phantom 4 UAV drone, equipped with a built-in camera, and Global Navigation Satellite System. Photos of the outcrop face and top were manually captured with an overlap of approximately 70% between each photo. Subsequently, the photos were imported into the software Agisoft Metashape® to generate a dense point cloud, and then to create the final triangular mesh. Digital outcrop models facilitate measurements, understanding of lateral and vertical relationships of sedimentary structures, integration of field data, construction of geological models, and remote description of inaccessible outcrops.

The fluvial architectural analysis relies on 275 palaeocurrents measurements obtained from individual cross-bedding foresets, and 266 measurements of dip angle and dip direction of sets and cosets basal bounding surfaces. These measurements were added to the software Stereonet (Allmendinger et al., 2012; Cardozo and Allmendinger, 2013), which automatically calculates the mean vector and circular variance.

The estimation of the mean original fluvial dune height (h_m), from cross-set thickness, helps access information regarding local flow depth variations (Leclair and Bridge, 2001; Reesink et al., 2015; Leary and Ganti, 2019; Li et al, 2022). In this study, the approach defined by Leclair and Bridge (2001) (Equation 1) was used, which is still being applied in recent works (e.g. Hartley and Owen, 2022; McLeod et al, 2023):

$$h_m = 2.9 * (\pm 0.7) * (S_m) \qquad (1)$$

where, S_m is the mean cross-set thickness. Before the application of Equation 1, a decompaction factor of 10% was applied to S_m (Hartley and Owen, 2022). This study is supported by 800 measurements of fluvial cross-set thickness. To calculate local flow depth (d), Leclair and Bridge (2001) defined:

$$6 < d/h_m < 10 \qquad (2)$$

Despite being imprecise, it can complement flow depth estimative calculated from channel-bar thickness (Leclair and Bridge, 2001; Hartley and Owen, 2022). Hartley and Owen (2022) excluded from their analysis abnormally thick cross-sets to avoid overestimation of channel depth. However, since the authors did not mention the method used to define such thickness threshold, in this study was used the

interquartile range method (IQR), a widely used statistical method to estimate data outliers, to define the upper bound (UB):

$$UB = Q3 + 1.5(Q3 - Q1) \quad (3)$$

where, $Q3$ is the value below which 75% of the data falls, and $Q1$ is the value below which 25% of the data falls. Data points above the UB are considered outliers, which corresponded to 3.8% of the cross-sets.

The use of 1D data is unreliable for estimating channel-depth because of the absence of architectural elements control. Moreover, core data tends to yield smaller estimations of true set thickness (Colombera et al., 2024). Nevertheless, since this was the only way to access a continuous succession of cross-sets, on a larger scale (c. 100 m), it was tested whether the thickness of cross-sets exhibited any vertical trend. Then, to evaluate the strength of identified trends, Spearman's rank correlation coefficient (Rs) was used (Davis 2002), where Rs = (+ or -) 1 means perfect correlation, and Rs = 0 means no correlation. To analyse if eventual correlations occurred by chance, the p-value approach was adopted (Davis 2002). The significance level for the calculated p-values was set at the commonly used threshold of 5%. In cases where the obtained p-value exceeds this threshold, it indicates that the observed correlation obtained by Rs is not representative and, thus, should not be upscaled. Rs and p-value were calculated using Excel ® functions. Furthermore, to evaluate the correlation of facies with granulometry, gravel content, and set thickness, the rank correlation coefficient Kendall's Tau-c (τ) was employed. Kendall's Tau-c (τ) effectively handles tied values in rank datasets (Kendall, 1938; Akoglu, 2018), as often seen with categorical sedimentology data. The degree of correlation (τ) was assessed based on Botsch (2011), categorizing the relationship strength between two variables as very weak (0 to 0.1), weak (0.1 to 0.19), moderate (0.2 to 0.29), and strong (0.3 or above).

Additionally, the cross-set thickness coefficient of variance (CV) is calculated to investigate if the fluvial bedforms were preserved in steady-state or disequilibrium conditions (Paola and Borgman, 1991; Leary and Ganti, 2019). The CV is only calculated when more than 30 cross-sets samples (Belle and Martin, 1993) are preserved within a channel unit (Lyster et al., 2022).

A classification related to gravel content within individual sets based on field descriptions is presented in Table 1, aiming to quantify the variations of gravel content within the LGV.

4. SEDIMENTARY FACIES AND THEIR ASSOCIATIONS

In the LGV, thirteen distinct facies were identified (Table 2). These facies are interpreted to have been accumulated in response to subaqueous or subaerial (wind-related) processes. They vary from fine- to very coarse-grained sandstones, well- to poorly- sorted, composed mainly of quartz, feldspar and lithoclasts, indicating subarkose to sublitharenite composition, with variable amounts of gravel (Table 1). These facies are arranged as the internal components of seven architectural elements developed within two distinct facies associations: fluvial channel facies

association (FC) and wind- and water-laid facies association (WWL). The FC is the dominant association, representing 93% of the total thickness measured for the LGV, whereas the WWL accounts for 7% (Fig. 2). The following sections present the main characteristics of each facies association, and their interaction with one another. Description and interpretation for individual facies are provided in Table 2.

4.1. Fluvial channel facies association (FC)

The fluvial channel facies association (FC) comprises seven sedimentary facies (Fig. 2) arranged in amalgamated, lenticular and tabular sets, and distributed in five architectural elements. The architectural elements are quantitatively detailed in figure 6, identified by their geometry, facies, palaeocurrent, and bounding surfaces of sets and cosets.

4.1.1. Facies and general characteristics

Trough cross-bedded sandstone (St) (Figs. 3A, 3C, and 3H) is dominant (73%) (Fig. 2), followed by low-angle cross-bedded sandstone (Sl) (13%) (Figs. 3E, 3F, and 3H), and sigmoidal cross-bedded sandstone (Ss) (12%) (Figs. 3B, and 3H). Planar cross-bedded sandstone (Sp), upstream dipping, with convex-up lamination, cross-bedded sandstone (Sad) (Fig. 3G), ripples cross-laminated sandstone (Sr), and laminated mudstones (Fl) are rare (Fig. 2). Facies Fl are preserved as discontinuous millimetre- to centimetre- scale layers between sets, draping an erosional surface, and occasionally, between foresets (Fig. 3C). However, mudstones are mainly preserved as mud clasts along cross-bedding foresets.

Facies Sl either form laterally extensive tabular deposits, or lenticular sandstone bodies with gentle concave-up basal surface. Convex-up lamination and parting lineation are associated. Typically, facies Sl transitions in a down-palaeocurrent direction to facies Ss through individual laminae traceable from the topset (horizontal/low-angle strata), to the toeset (concave-up strata) (Figs. 3B, and 9B). This horizontally to low-angle stratified topset may exhibit finer grain size, and less gravel content, than the down-palaeocurrent direction foresets. Facies Sl is included in facies Ss when this lateral relationship is evident. The transitions between facies Sl, Ss and St within the same bed also occur without the relationship mentioned above (Fig. 4). In such cases, they are defined as separated facies.

Most FC sandstone bodies record medium-grained sandstones (51%), followed by coarse-grained sandstones (36%), and a weak correlation between facies and granulometry is observed (Fig. 5A). It presents an overall bimodal character of sediment load, composed of gravel and sand. Bimodal is used in this case in a broad sense, when pebbles are in a sandy matrix without clasts of intermediate sizes (Steel and Thompson, 1983). Gravel clasts, mostly composed of milky quartz and quartzite, range from sub- to well-rounded, with low- to high-sphericity. Slightly gravelly sandstone (Table 1) dominates the gravel content classes (Fig. 5B). Granule to pebble clasts are concentrated along the foresets of facies St (Fig. 3A) and Ss (Figs. 3B, and 9B), occasionally at the set base. Similarly, rounded or angular mud clasts, up to 35 cm in diameter along their primary axis, may be concentrated as breccias directly above the bases of sets (Fig. 3D). Facies Sl exhibits the lower content of

gravel, followed by facies Ss and facies St, respectively, which is confirmed by the strong correlation coefficient between facies and gravel content (Fig. 5B)

Cross-set thickness distribution throughout the entire FC deposits, has a median value of 30 cm (Fig. 5C). A weak correlation is observed between facies and cross-set thickness (Fig. 5C). Palaeocurrent data indicates a prevailing palaeocurrent to northeast, with varying circular variance depending on the architectural element (Fig. 6), as detailed in the following sections.

Core data revealed a thinning-upward trend of cross-set thickness (Fig. 15B) in the upper part of the LGV. When all cross-sets are considered, no correlation is observed between cross-set thickness and depth (Rs= 0.07; *p*-value = 0.06) (Fig. 15B). However, when the analysis is constrained to cross-sets thicker than 50 cm, a strong correlation is observed (Rs = 0.61; *p*-value = 0.005) (Fig. 15B). Therefore, the occurrences of relatively larger cross-sets tend to decrease towards the top of the LGV.

The upper and lower boundaries of the FC are identified upon contact with the wind- and water-laid facies association (WWL). The basal contact is slightly erosive, truncating the WWL below at a low angle. The upper contact may be preserved as a flat, or an undulating surface, the genesis of which is further discussed in section 4.2.1. Herein, the term “complete FC unit” is used descriptively, when both, lower and upper boundaries, are recognised. Table 3 presents quantitative data on architectural elements proportions of individual complete FC units. Figure 5D displays the overall thickness distribution of complete FC units, observed in outcrops and in the core. The occurrence of multistorey amalgamated and tabular sandstone bodies, bounded by erosive surfaces, and predominantly consisting of medium- to coarse-grained sandstones, well- to poorly-sorted, with mud clasts, gravel, and unidirectional cross-strata, indicates deposition in a fluvial channel (Collinson, 1996), with palaeocurrent to the north-east, in agreement with previous studies (Perriaux, 1961; Gall, 1972; Durand, 1978; Dachroth, 1985; Ghienne et al., 1994; Bourquin et al., 2009).

The dominance of facies St indicates that the FC records essentially the migration of 3D dunes (Miall, 2006) under lower-flow regime conditions (Zellman et al., 2021). However, one-quarter of the FC consists of facies Ss and Sl (Fig. 2), revealing significant occurrences of transitional (Røe, 1987; Wizevich, 1992; Fielding, 2006; Walker and Holbrook, 2023) to upper-plane beds (Hjellbakk, 1997; Fielding, 2006; Plink-Björklund, 2015). Facies Ss may represent the original bedform morphology (Røe, 1987; Fielding, 2006; Collinson et al., 2006), with the preserved convex-up shape at the crest, a consequence of rapid net vertical aggradation, preventing significant erosion due to high sediment load (Røe, 1987; Hjellbakk, 1997). Distinguishing sigmoidal stratification (facies Ss) in terms of Froude-number (Fr) flow conditions might be impossible, due to the wide range of circumstances in which facies Ss may occur (Ghienne et al., 2010; Plink-Björklund, 2015; Lang et al., 2021). Similar challenges apply to facies Sl (Yagishita et al., 2004; Ohata et al., 2022), whenever diagnostic features of Froude-supercritical flow, such as parting lineation and convex-up laminations, are not found. Thus, the classification based on the direct relationship between these sedimentary facies and Froude-number reaching supercritical conditions (Fr > 1) is avoided. Ss and Sl facies are interpreted based on

Southard's (1991) diagram, as upper-plane beds for facies Sl, and transitional cross-bedding from 3D dune (St) to upper-plane bed for facies Ss.

The vertical and lateral intermixing of facies St, Ss, and Sl may be related to river discharge variability (DeLuca and Eriksson., 1989; Fielding, 2006; Miall, 2006; Plink-Björklund, 2015), changes in sediment supply, or spatial flow fluctuations (Røe, 1987; Hjellbakk, 1997; Zellman et al., 2021). Discharge variability is evidenced, for instance, by the presence of facies Fl between cross-bedded sandstone sets (Fig. 3C), and along foresets, which indicate ephemeral flows, subjected to rapid waning of floods (Miall, 2006; Plink-Björklund, 2015). Conversely, spatial flow fluctuation is observed in the downstream transition from low-angle topset to concave-up toeset of facies Ss, where the topset is affected by upper-flow regime, and the toeset by lower-flow regime (Hjellbakk, 1997). The concentration of coarser grains, and gravels, in the down- palaeocurrent direction foresets, compared to the topsets, indicates that coarser sediments rolled over the bedform to accumulate by settling and avalanching on the slipface (Sauderson and Lockett, 1983). Distinct evidence to support temporal or spatial flow variations is presented further.

The consistent occurrence of a smaller proportion of gravel content in facies Sl, followed by facies Ss and St (Fig. 5B) highlights an apparent inverse relationship between gravel content and flow regime, which is confirmed by the strong correlation coefficient between facies and gravel content (Fig. 5B). This is explained by the overpassing process (Allen, 1983b), which occurs in bimodal grain-size-distribution sediment load. At upper-flow regime and high shear-stress conditions, the large sub- to well-rounded gravel rolls over a firm bed of close-packed sand grains, (Allen1983b; Carling, 1990), depositing downstream where flow conditions change. In some cases, this process has been related to strong flashy floods events (Allen, 1983b).

Rare occurrences of antidunes (Sad) indicate moments when channel flow reached supercritical conditions (Fielding, 2006). These facies can form and be preserved in shallow flows that rapidly reach Froude number equal to 1, or during extreme major flood events followed by rapid drop in water level (Fielding, 2006; Fielding et al., 2018). As these structures tend to be reworked during waning flow conditions (Miall, 2006; Myrow et al., 2018), preservation potential is low, making these deposits underestimated in the rock record.

4.1.2. Aggradational architectural element (AE)

The aggradational architectural element (AE) (Fig. 7) is the predominant architectural element within the FC (Fig. 5E). It has an erosional base, showing, in a dip-section, a downstream dip (<15°), where large (c. up to 35 cm) mud clasts are commonly concentrated. Gravelly sandstones (GS) lenses also often occur at the base of the elements. The AE comprises tabular (Fig. 7A) and amalgamated (Fig. 7B) sets of facies St, Ss and Sl (Fig. 7B), occasionally featuring discontinuous facies Sp, Sad, Sr, and Fl. The internal sets are bounded by horizontal to concave-up surfaces, sometimes erosional. Locally, it preserves thinning-upward trends, aligning with the observations of Ghienne (1994).

The coefficient of variance (CV) of cross-set thickness, calculated where more than 30 cross-set samples are preserved in the same architectural element, of a complete FC unit (LGV3, LGV7, and LGV9) (Table 3), presented a mean value of 0.5.
The AE is interpreted as the aggradation and coalescence of 3D (St), humpback, and washout dunes (Ss and Sl), within flat and wide channels, or atop large bars (Hjellbakk, 1997; Scherer et al., 2015). Thinning-upward sequences register the final stages of channel infills (Ghienne, 1994) or top of bars (Li et al., 2015). This architectural element corresponds to Hjellbakk's (1997) dune complexes (DC), or a combination of Miall's (1988) sandy bedforms (SB) and channel element (CH). Basal surfaces with angular mud clast breccia (Fig. 3G), suggest the erosion of semi-consolidated mud cracks, originating from sub-aerially exposed mud layers within ephemeral channels (Bridge, 2003; Bourquin et al., 2009), during flow stage fluctuations (Miall, 1988). It is not clear whether some channels experienced ephemeral flow while perennial channels were still active, or if the flow was intermittent in all channels. However, evidence of ephemeral flow is commonly recorded across the FC, leading to the possibility of an intermittent fluvial system. The statistical distribution of set thickness in the AE element (Fig. 5F) indicates disequilibrium conditions induced by discharge variability (Myrow et al., 2018; Leary and Ganti, 2019; Colombera et al., 2024), and the CV may suggest abrupt waning-flow conditions associated with such variabilities (Myrow et al., 2018; Leary and Ganti, 2019). *4.1.3. Downstream accretion architectural element (DA)*

The downstream accretion architectural element (DA) (Fig. 8A) is characterised by horizontal to undulating basal surfaces, composed of sets of facies St and Ss, bounded by surfaces dipping at angles ranging from 3° to 18° in the same direction, or obliquely (<60°), to the cross-bedding foresets direction (Fig. 6).

The DA is interpreted as middle-channel bars formed by superimposed dunes (Allen, 1983a; Miall, 1988; Scherer et al., 2015). The presence of facies Ss indicates flows that locally, or temporally, reached the transition between dune and upper-plane bed stability field during the bar migration (Røe, 1987; Fielding, 2006).

4.1.4. Trough simple architectural element (TSE)
The trough simple architectural element (TSE) (Fig. 8B) is defined by horizontal to sub- horizontal basal surface. It consists of individual tabular sets of facies St, ranging between 45 cm to 1,8 m thick, with a lateral extension of tens of metres when viewed in a dip-section.

The TSE is interpreted as unit bars (Røe, 1987; Hjellbakk, 1997), deposited under steady-state flow conditions (Røe, 1987), with minor flow pulsations revealed by the reactivation surfaces (Røe, 1987). It may also represent large-scale 3D dunes (Miall, 2006). Distinguishing between unit bars and large dunes is challenging in channel-dominated deposits with undefined channel margins (Miall, 1988; Skelly et al., 2003), especially in the context of variable flow depths and discharge (Herbert et al., 2019).

4.1.5. Sigmoidal simple architectural element (SSE)
The sigmoidal simple architectural element (SSE) (Fig. 9) is defined by horizontal to sub- horizontal basal surface, composed of individual tabular sets of facies Ss, ranging between 45 cm to 1,8 m thick, with lateral extension of dozens of metres. It commonly presents aggradational foresets, and reactivation surfaces (Fig. 9B).

When SSE is composed of gravelly sandstone (Table 1), gravel clasts are concentrated in the lee side, generally absent in the horizontal to low-angle stratified topset (Fig. 9B). Sometimes more than one SSE element may stack (Fig. 9A).

The SSE is interpreted as a humpback bar, product of single flood events of heavily suspension-laden currents in the transition from upper to lower-flow regime (Allen, 1983; Røe, 1987; Hjellbakk, 1997; Manna et al., 2021), within a shallow, high-energy channel (Hjellbakk, 1997). Occurrences of isolated SSE indicate abrupt temporal changes in flow conditions (Røe, 1987). The absence of gravel in the low-angle topsets, while they are abundant in coeval foresets, is addressed to gravel overpassing (Allen, 1983b), due to local upper-flow regime conditions at the top of humpback bars (Allen, 1983b; Carling, 1990), and concentrating in the lee side, which is affected by lower-flow regime conditions (Hjellbakk, 1997). When more than one set of SSE is stacked, it suggests the increase of flow depth sufficiently deep to permit deposition as cosets (Røe, 1987; Carling, 1990).

4.1.6. *Laminated sand sheet architectural element* (LS)
The laminated sand sheet architectural element (LS) (Fig. 9A) is composed of laterally extensive, tabular sandstone packages, locally presenting pinch-out edges, ranging between 30 cm and 1.95 m thick, almost exclusively of facies Sl. Records rare facies Ss and St as isolated lenses, and facies Sm and Sr at the top. It is the architectural element with lower gravel content within the FC (Fig. 6), and rarely is formed by coarse-grained sandstone (Fig. 6).

The LS indicate shallow floods under upper-flow regime conditions (Fielding, 2006; Miall, 2006), filling in ephemeral channels (Miall, 2006). When pinch-out edges are present, they are interpreted as formed on the stoss-side of unit bars (Alexander et al., 2020). The local presence of facies Sm and Sr at the top represents fast waning flow and/or high sediment concentration in the final depositional stages (Allen and Leeder, 1980). The lower gravel content is attributed to the overpassing process (Allen, 1983b), and the lack of occurrences of coarse-grained upper-plane bed aligns with observations of Núñez-González and Martín-Vide (2010), which indicates that, in coarse grain sizes, the dune phase can be followed by antidunes, with no transitional plane bed stability.

4.1.7. Interactions between FC architectural elements

These architectural elements can evolve down-dip. Figure 4 illustrates LS transitioning in a down-palaeocurrent direction to TSE. These transitions are commonly marked by reactivation surfaces zones between the elements (Fig. 4). Simple elements (TSE and SSE) can also evolve down-dip to DA (Fig. 13). The inverse transition is also observed, which is identified by other authors as a transitional element (Hjellbakk, 1997; Manna et al., 2021). Recognising all these transitions demands down-dip exposure and extensive outcrops. The downstream transition between LS and TSE, within the same bed (Fig. 4), suggests flow pulsations (Røe, 1987; Miall, 1988) and/or changes in channel cross- section geometry during bedform migration (Bridge, 2003). For instance, LS indicates lower confinement compared to TSE, or shallower conditions in the channel (Miall,

2006). The presence of reactivation surfaces between the elements suggests flow pulsations (Røe, 1987). The downstream transition from simple elements, TSE and SSE, to DA, indicates the coalescence of unit bars to form larger compound bars, a result of either increasing discharge, or a decrease in riverbed gradient (Li et al., 2022). The top surface of TSE, when in contact with the AE, is often eroded, dipping upstream at a low angle (Fig. 8B). This is also observed in relatively larger, isolated, cross-sets within the AE, when underlying smaller cross-sets (Fig. 7B). Both cases are interpreted as the partial cannibalisation of large bedforms due to disequilibrium during a rapid decrease in flow (Myrow et al., 2018). These smaller sets could be considered low- discharge channels situated between mid-channel bars, while the isolated large sets within the AE, and the architectural elements TSE, SSE, and DA are indicative of high- discharge channels (Skelly et al., 2003). The higher palaeocurrent circular variance of cross-sets within the AE, compared to the other elements (Fig. 6), indicates increased sinuosity (Galeazzi et al., 2021) in the former, supporting the interpretation of cross-sets preferentially formed inside low-discharge channels, migrating between braided bars. *4.1.8. Channel depth estimation*

To estimate the low-discharge channels' mean flow depth, only sets within AE elements were used. Sets thicker than 78 cm (3.8% of the dataset), were considered outliers by the IQR method (Equation 3), and then excluded from the analysis to avoid overestimations (Hartley and Owen, 2022). A total of 251 sets remained.

Results revealed a range of mean original dune height (H_m) (Equation 1) varying from 64 cm to 1.05 m. Concerning low-discharge mean flow depth (d) (Equation 2; Leclair and Bridge, 2001), values range from 3.8 to 10.5 m. Such imprecision was anticipated (Leclair and Bridge, 2001; Reesink et al., 2015), and the lack of complete bar thickness recognition does not allow a finer calibration, as it would approximate the bank-full channel depth (Skelly et al., 2003; Bridge, 2003; Hartley and Owen, 2022).
To evaluate the potential impact of mixing different fluvial genetic units (Bourquin et al., 2006; 2009), individual d is also calculated by outcrop. In instances where a complete FC unit is exposed, the analysis is restricted to AE within its limits to constrain possible temporal variabilities of the system. Results (Table 3) showed a range of H_m from 24 cm to 1.43 m, and d from 1.5 m to 14.3 m. Nevertheless, most outcrops exhibited H_m and d within the values calculated using the entire AE dataset, suggesting no substantial changes, in terms of low-discharge flow depth, recorded across the studied outcrops of the LGV.
Although 1D data were not utilised to estimate channel depth, the observed reduction in the frequency of larger cross-sets (c. > 50 cm in thickness), towards the top of the LGV (Fig. 15B), is interpreted as the result of diminishing channel depths and/or a decline in the incidence of high discharge fluvial events.

4.2. Wind- and water-laid facies association (WWL)

This facies association comprises eight sedimentary facies, interdigitated laterally and vertically on a centimetre to decimetre scale. The facies are distributed in two architectural elements: the hybrid sand sheet (HSS) and aeolian dune (AD), which descriptions and interpretations are presented in sections 4.2.2. and 4.2.3., respectively. The choice to combine aeolian dunes and sand-sheet deposits into the

same facies association is made due to the limited prevalence of the WWL within the Lower Grès Vosgien Formation.

4.2.1. Facies and general characteristics

This facies association is composed mainly of fine- to medium-grained sandstone (Fig. 11B), well- to poorly-sorted. Granules and pebbles may be present mainly constrained to one surface as a lag deposit (Dixon, J.C., 2014). The WWL exhibits flat base deposits of greater extent that the maximum width of the individual outcrops in which they are observed (c. 100 m) (Fig. 13), occasionally being eroded out laterally by overlying FC (Fig. 13). Facies trough cross-bedded sandstone with grain-flow laminae (Sta) (Figs. 10D and, 10E), adhesion structures (Sa) (Fig. 10C), wave ripples (Sw) (Figs. 10B, and 10C), microbially induced sedimentary structures (Mb) (Fig. 10B), massive sandstone (Sm), and rare Fl, interdigitate laterally and vertically.

The lower boundary of the WWL is horizontal to sub-horizontal and abrupt, occasionally undulating, most frequently bounded by a lag deposit, with pebbles (Figs. 10D, 10E, and 10F), commonly faceted, displaying the same composition and sizes as those present within the FC. The gravel content can be arranged scattered in a single surface, or tightly packed and commonly embedded in a sandy matrix. Although most of these surfaces are overlain by facies composing the WWL, in some cases, overlying fluvial deposits present erosive contact with the WWL and are conformable with the lag surface. Thus, in these cases, the lag deposit bound two fluvial deposits (see Architecture 5 in Figs. 12B, and 12F). Figure 10B exhibits the overall thickness distribution of the WWL, observed in outcrops and core. Core data record thicker WWL towards the top of the LGV (Fig. 15D), in which a weak negative correlation is observed between WWL thickness and depth (Rs = - 0.36). However, the *p*-value of 0.12, above the significance level of 0.05, indicates that in the dataset there is not enough evidence to correlate WWL thickness and depth.

The first evidence of interruption of fluvial processes and establishment of WWL is the basal lag surfaces, interpreted as sand-drift surfaces formed when unsaturated winds eroded subaerially exposed fluvial deposits, leaving behind a deflation lag (Clemmensen and Tirsgaard, 1990) (Fig. 12A). Faceted pebbles are interpreted as ventifacts (Durand and Bourquin, 2013). Planar sand-drift surfaces indicate deflation down to the water- table level (Havholm and Kocurek, 1994), and when undulating, it is interpreted as regions where deflation did not reach the water-table level (Gross, 2022). Where gravel clasts on sand-drift surfaces are tightly packed, and embedded in a sandy matrix, it suggests rework by ephemeral subaqueous flows (Fig. 12A) before the deposition of the overlying WWL. The resistance of sand-drift surfaces to erosion (Fig. 12F) may indicate early cementation, a common feature associated with sediments exposed to water-table level fluctuations (Fryberger et al., 1988; Fryberger, 1991).

Aeolian origin was attributed when at least two of the following criteria were observed: inverse graded lamination (Clemmensen and Abrahamsen, 1983), absence of gravel content, pin-stripe lamination (Fryberger and Schenk, 1988), granule ripples (Fryberger et al., 1992), and a laterally extensive deflation lag at the set base (Clemmensen and Tirsgaard, 1990).

4.2.2. Hybrid sand sheet architectural element (HSS)

The hybrid sand sheet architectural element (HSS) consists of tabular deposits with thickness varying from 7 cm to 1.85 m, with a median value of 35 cm (Fig. 11C), and a mean of 44 cm. It is composed of fine-grained sandstone, poorly- to well-sorted, with centimetre-scale interbedded facies Sla, Sa, Sw, Sm and Mb (Figs. 10B, and 10C). Bleaching is recurrently observed in HSS, both in outcrop and core (Figs. 10B, 10F, 12C, 12E, and 12F), sometimes making it difficult to distinguish facies. Occasionally, an upward trend of stacked facies Sla, Sa (and/or Mb), and Sw is recognised (Figs.10B, and 10C). The contacts between facies are conformable. The HSS presents a sharp horizontal lower surface when overlying AD deposits.
The hybrid sand sheet architectural elements are composed of features that suggest the presence of water during their deposition (Fig. 14A), such as facies Sa (Kocurek and Fielder, 1982), Sw (Ribes, 2015), Mb (Gerdes, 2007; Basilici et al., 2021), and the occasional occurrence of Fl and gravel clasts (Miall, 2006). Additionally, facies Sla indicate occasions of dry sediments being deposited as translatent strata (Hunter, 1977; Cain and Mountney, 2009). The centimetre-scale intercalation of facies Sla, Sa, Sw, and Mb is interpreted to be mainly controlled by the balance between water-table level fluctuation and the rate of aeolian sediment supply (Clemmensen, 1991; Havholm and Kocurek, 1994; Carr-Crabaugh and Kocurek, 1998) (Fig. 12A). These characteristics indicate deposition in the context of an aeolian sand-sheet (Clemmensen, 1991; Trewin, 1993; Basilici et al., 2021; Cosgrove et al., 2022; Gross et al., 2022). However, the term "hybrid" is used because of the dominance of water-related processes.

4.2.3. Aeolian dune architectural element (AD)

The aeolian dune architectural element (AD) consists of tabular to concave-up base deposits of facies Sta and Sla. Individual AD records thickness varying from 10 cm to 2.73 m, with a median value of 78 cm, and a mean of 84 cm (Fig. 11C). It can be preserved as a single set (Figs. 10D, 10E, 12C, 12G, and 12H), or with two sets (Fig. 12D). Foresets predominantly dip towards the north-northeast (Fig. 11E), with a maximum preserved dip angle of 20°, and transition downward to facies Sla (Figs. 12C, and 12D). Where they overlie HSS, the AD often lay above shallow erosional surface dipping in the same direction as the foresets of facies Sta (Figs. 10E, 12C, 12G, and 12H).

The AD represents 60% of the total WWL thickness. However, in terms of occurrences, it represents 43% (Fig. 11D). The aeolian dune architectural element record sedimentation via the wind as migrating aeolian dunes (Hunter, 1977; Clemmensen and Abrahemsen, 1983; Kocurek, 1991; Scherer, 2000) (Fig. 14B). Accumulation of superimposed sets occurs via aeolian climbing dunes (Clemmensen and Abrahemsen, 1983; Kocurek, 1991). Considering the maximum dip angle measured from grain-flow strata of 20°, and the angle of repose of modern aeolian dunes, typically between 32° and 34° (Bristow and Mountney, 2013), it is interpreted that only the lowermost part of the dunes has been preserved. The shallow erosional surface at the base of the AD, in contact with HSS (Figs. 10E, 12C, 12G, and 12H), is interpreted as blowout hollows (Hesp and Walker, 2013) formed before the wind saturation with sand. This deflation process was followed by wind saturation, dune accumulation, and dune migration above these surfaces (Figs. 12A, and 14B).

4.2.4. Interactions between WWL architectural elements

Regarding the vertical arrangement of the architectural elements, the WWL records four main preserved architectures. The most frequently preserved architecture is composed solely of HSS (architecture 4 in Figs. 12B, 12E, and 12F), which also exhibits the thinnest preservation (Fig. 12I). The second most common architecture features HSS overlain by an AD, with a blowout hollow surface in between, followed by another HSS overlying the AD (Architecture 1 in Figs. 12B, 12C, and 12G). Occasionally, the upper HSS from this architecture is absent, possibly due to erosion from the subsequent fluvial process, which then records only a HSS overlaid by AD (Architecture 2 in Figs. 12B, and 12H). The fourth preserved architecture is characterised by the presence of only AD.

Figure 12I illustrates that the thickest architectures are associated with AD, despite the prevalent occurrences of HSS (Figs 11D, and, 12B). These vertical architectures may evolve laterally between each other on an outcrop scale (Fig. 13).

4.3. Lateral and vertical interactions between facies associations

Figure 13 illustrates two levels of WWL displayed with a complete FC unit, of 12.8 m (Table 3), in between. The lower WWL level (number 3 in Fig. 13) present greater extent that the outcrop width, however, its thickness decreases laterally in a down-palaeocurrent direction of the overlying FC. The upper WWL level (number 4 in Fig. 13) also presents a thickness decrease following the palaeocurrent direction and; in this case, the entire WWL is laterally eroded by the overlying FC.

The outcrop LGV13 records the lower contact with Permian deposits (Bourquin et al, 2009). Thus, outcrops LGV13, LGV9, and LGV10 (see Fig1A for location), which are vertically stacked, represent the lower part of the LGV. Despite sections covered in between, combined they record 70 m of outcrop without WWL, indicating the absence, or relatively minor occurrences, of WWL in the lower part of the LGV. The core section described represents the upper 100 m of the LGV (Aichholzer, 2019). Core data record 13 occurrences of WWL, intercalated with FC, in the upper 76 m (Fig. 15). The frequency of intercalations increases upwards, while the FC thickness decreases. This is supported by the strong correlation between depth and FC thickness (Rs = 0.71; *p*-value = 0.049) (Fig. 15C).

5. DISCUSSION

5.1. Fluvial channel facies association (FC) depositional controlling factors

The distribution of lower-, transitional-, and upper-flow regime sedimentary structures can be attributed to spatial effects, particularly highlighted by varying flow depths across humpback bars. The upper part of such bars, characterised by shallower water, records upper-flow regime conditions, whereas the lee-side, characterised by deeper flow depths, records lower-flow regime conditions. However, when these facies are associated with reactivation surfaces, gravelly sandstone lenses, mud clasts breccias, and evidence of ephemeral channels, such as mud draping sets and foresets, it indicates that discharge variability was also a controlling factor during the deposition of the FC (Miall, 1988; DeLuca and Eriksson, 1989; Bhattacharyya and Morad, 1993; Fielding, 2006; Miall, 2006; Fielding et al., 2009; Plink-Björklund, 2015; Fielding et al, 2018; Alexander et al., 2020; Arévalo, et al., 2022). The dominance of

small dunes, and unit bars with signs of modification over time, indicates a system that was subjected to moderate discharge variability (Fielding et al., 2018). Rapid flow recession, associated to such discharge variabilities, is evidenced by (i) isolated SSE (Røe, 1987), (ii) Fl between cross-bedding sets and foresets (Miall, 2006; Plink-Björklund, 2015), (iii) antidunes (Fielding, 2006; Fielding et al., 2018), (iv) signs of cannibalisation of large bedforms (Myrow et al., 2018), and (v) the coefficient of variance (CV) of AE cross-set thickness (Table 3) (Leary and Ganti , 2019).

An equivalent to the FC can be made with observations by Skelly et al. (2003) in a modern aggrading braided river. The authors defined two main scales of channel elements, that alternate through time. Firstly, a channel complex active at low discharges, composed of small-scale dunes migrating between mid-channel bars. Secondly, a single channel active at high discharges, which contains not only large- and small-scale dunes, but also braided bars with height in the order of the bank-full channel depth. In the FC deposits of the LGV, the relatively low-discharge channel is represented by the sets within the AE deposits, and the high-discharge channel is represented by isolated larger sets within the AE and by the elements TSE, SSE and DA.

5.2. Wind- and water-laid facies association depositional controlling factors

When the rate of water-table rise was balanced with sediment supply, the conditions were favourable for depositing dry sediments in the form of facies Sla (Carr-Crabaugh and Kocurec, 1993; Scherer and Lavina, 2005). Alternatively, a damp surface could have been formed by the interception of the capillary fringe, then facies Sa (Kocurek and Fielder, 1982; Trewin, 1993; Mountney et al., 1999) and Mb (Fryberger et al., 1988; Gerdes, 2007; Rodríguez-López et al., 2014) were deposited (Figs. 12A, and 14A).

The presence of facies Sw suggest that the depositional surface was locally submerged, creating ephemeral ponds (Clemmensen, 1991; Carr-Crabaugh and Kocurec, 1993; Trewin, 1993; Basilici et al., 2021) (Fig. 14A). The absence of facies Fl, or any subaqueous transport structures associated with such ponds, implies that they were formed when the rate of water-table rise outpaced the sediment supply (Trewin, 1993; Basilici, et al., 2021) (Fig. 12A). Alternatively, another process responsible for generating such ephemeral ponds are sheet-flood events reaching the sand-sheet and related landforms (Clemmensen, 1991; Veiga et al., 2022; Ghinassi et al., 2004; Scherer and Lavina, 2005; Miall, 2006; Paim and Scherer, 2007; Bristow and Mountney, 2013; Al- Masrahy and Mountney, 2015) (Fig. 14A). In the latter, Sw is capped by a Fl laminae, indicating subsequent calm sedimentation (Miall, 2006). Ephemeral flood events are evidenced by gravel-size clasts, often aligned on a surface within the WWL, with no other subaqueous flow structures associated. This suggests wind winnowing processes that followed the ephemeral flood, leaving behind a deflation lag within the WWL facies (Figs. 12A, and 14B).

The lateral facies distribution within the hybrid sand sheet architectural element (HSS) was influenced by local topography, leading to distinct interactions between the water- table level and the depositional surface (Fig. 14A). The upward transition between facies Sla, Sa (and/or Mb) and Sw (Figs. 10B and, 10C), respectively, record the gradual outpace of water-table rise against sediment supply (Trewin, 1993; Basilici, et al., 2021). The accumulation of aeolian dunes requires the

availability of a substantial volume of sand for aeolian transport (Basilici et al, 2021) (Fig. 12A), and aeolian dune preservation in otherwise fluvial dominated environments typically requires a continuous increase in the relative water-table level (Scherer and Lavina, 2005; Basilici et al, 2021). The growth of aeolian dunes is associated with events of water-table level fall, which generates the blowout hollows concomitant to the increase of dry sediments available for the wind to transport (Figs. 12A, and 14B). Thus, the AD and HSS deposits took place during distinct temporal moments (Fig. 14).

The common preservation of HSS, compared to AD (Fig. 11D), is associated with a system that experienced a persistent scarcity of fine-grained dry sand available (Trewin, 1993; Al-Masrahy and Mountney, 2013), combined with ephemeral floods able to remobilise them (Kocurek and Nielson, 1986; Langford, 1989; Clemmensen, 1991) (Fig. 12A). This scarcity can be attributed to (i) a sediment source area originating from inactive fluvial deposits, with a limited budget of available fine-grained sand (Fig. 5A) (Trewin, 1993; Mountney et al., 1999), (ii) constrained sediment transport distances due to active fluvial channels nearby (Trewin, 1993; Farraj and Harvey, 2004), and (iii) the repeated intersection of the water-table with the depositional surface, potentially inhibiting aeolian sediment transport (Langford, 1989; Carr-Crabaugh and Kocurek, 1993; Trewin, 1993; Scherer and Lavina, 2005).

5.3. Large-scale depositional system

Although this study mainly focuses on the fluvial and aeolian architecture, certain characteristics suggest the LGV as part of a fluvial fan system (distributive fluvial system – DFS/ megafan). The overall retrogradational context during the deposition of the Middle Buntsandstein (Bourquin et al., 2006; 2009), and the upward tendency for cross- set thickness decrease (Fig. 15B), may suggest shallower channels in the distal parts of the system. Despite the uncertainties of using 1D data to analyse cross-set thickness, this is a characteristic expected in DFS (Hartley et al., 2010; Weissmann et al., 2015; Ventra and Moscariello, 2023). Also, the upward increase of interactions between FC and WWL might indicate an increase in avulsion frequency in more distal parts of the fluvial system, supporting the DFS hypothesis (Brookfield, 2008; Hartley et al., 2010; Weissmann et al., 2015; Reis et al., 2022). Furthermore, other general aspects observed in the LGV also support the DFS interpretation. These include: (i) the correlation between fan formation and discharge variability (Leier et al., 2005; Hansford and Plink-Björklund, 2020; Ventra and Moscariello, 2023), where dynamic channel aggradation, and avulsion, result in a complex interfingering of channelised and sheet like deposits (Davidson et al., 2013), extending laterally for tens of kilometres (Miall, 2006), (ii) most of the modern DFS dissipate into aeolian systems (Hartley et al., 2010), forming aeolian sand-sheet deposits (Cain and Mountney, 2009), and interfingered sheet-floods with aeolian facies (Brookfield, 2008), and (iii) the hypothesis that DFS/megafans present the most efficient preservation potential among fluvial systems (Ventra and Moscariello, 2023), as the LGV records c. 200 m of fluvial-dominated sediments, deposited in about 1.8 m.y. (Bourquin et al., 2006; 2009).

Despite the common progradational trends (regressive context) observed in most fluvial fan systems (Weissmann et al., 2015; Wang and Plink-Björklund, 2019),

examples of fluvial fans systems formed in a retrogradational context have also been documented (Cain and Mountney, 2009; Kukulski et al., 2013).

The coverage of the study area is restricted in terms of large DFS (megafans) scale. Thus, tendencies of lateral changes of channel dimensions, amalgamation, grain size, or floodplain preservation, often considered characteristics of DFS (Hartley et al., 2010; Weissmann et al., 2010; Hartley and Owen, 2022), were not observed. Moreover, the upward decrease in cross-set thickness presented in figure 15B, considered a characteristic of a retrogradational DFS, is based on 1D data, which carries uncertainties in correlating set thickness with dune size and, consequently, channel depths (Colombera et al., 2024). These aspects, associated with the possible overlap of characteristics between DFS with those of tributary fluvial systems (Sambrook Smith et al., 2010; Fielding et al., 2012), highlight that further studies covering the entire Buntsandstein Group, especially laterally extrapolating the study area, are necessary for a conclusive characterisation.

Bourquin et al. (2009) applied sequence stratigraphy concepts to the LGV, categorising the sand-drift surfaces as instances of base-level fall associated with climatic events, correlatable between outcrops regionally, and across the western part of the German Basin. However, in the context of the DFS hypothesis, major channel belt avulsions emerge as an alternative interpretation for the local absence of fluvial deposition, and, consequently, the development of these surfaces and the accumulation of WWL (Langford and Chan, 1989; Cowan, 1993).

The lack of evaporate deposits, the abundant water-related facies, and the already arid climate during the FC deposition (Peron et al., 2005), raise the question if the WWL, above the sand-drift surface, were deposited in different climatic conditions compared to the FC. Evidence indicates that the accumulation of WWL may have occurred concomitant with fluvial deposition. Given the close relationship between groundwater level, in braid plain, and river stages (Banks et al., 2022), the high-frequency intercalation of high and low water-table levels, observed within the HSS, could directly correspond to fluvial interannual high and low discharges, respectively. The ephemeral floods in HSS may be linked to crevasse-splay, a common feature in braided rivers preceding channel avulsion, during peak discharges (Ethridge et al., 1999). The limited availability of dry sand during HSS deposition aligns with the presence of relatively nearby active fluvial channels (Clemmensen, 1991; Trewin, 1993). Furthermore, the lowering of the water-table level, leading to the formation of blowout hollows and accumulation of aeolian dunes, indicates climatic (temporal) events at a lower frequency compared to those observed within the HSS. These events may be coeval with periods of ephemeral fluvial activity, as recorded by the laminated sand sheet elements, and by mud deposited between sets and foresets. The variable preservation thickness of WWL, ranging from a singular sand-drift surface to three metres, indicates the spatially distinct re-establishment of fluvial deposition. This, coupled with the slight erosional relationship between FC and the underlying WWL, also leads to channel avulsion interpretation (Hajek et al., 2010). However, this alternative interpretation carries uncertainties, such as: (i) the lack of timescale control in the FC and WWL dynamics, to precisely evidence their contemporaneity, (ii) the unknown periodicity of avulsions in large DFS (megafans) (Wilkinson and Gunnell, 2023), and (iii) since avulsions (autogenic) may also be influenced by climatic (allogenic) events, differentiating them in the rock record

becomes challenging (Ventra and Clarke, 2018). Despite climatic or channel avulsion controlling the FC and WWL intercalation, complete WWL and sand-drift surfaces can be laterally eroded at the outcrop scale (Fig. 13). Thus, caution must be taken when extrapolating these surfaces beyond the scale of hundreds of metres, especially in the same direction of the fluvial palaeocurrents.

6. CONCLUSIONS

Two facies associations compose the Lower Grès Vosgien Formation (LGV): fluvial channel (FC) facies association, comprising 93% of the total thickness measured for the LGV, and wind- and water-laid facies association (WWL), which accounts for 7%. The FC records 75% of its thickness by lower-flow regime sedimentary structures, and 25% by transitional- and upper-flow regime sedimentary structures, deposited in shallow, sometimes ephemeral, and poorly confined, braided channels. The WWL records 60% of its thickness by aeolian dunes (AD), and 40% by hybrid sand sheets (HSS). However, in terms of occurrences, the HSS represents 57% of the WWL, while the AD, 43%, which indicates the persistent presence of water during the WWL deposition.

The distribution of lower-, transitional-, and upper-flow regime sedimentary structures, in the FC, provides evidence of temporal and spatial flow variabilities, sometimes making it challenging to distinguish between them. Spatial effects in flow variability are exemplified by the overpassing process that removes gravel from the top of humpback bars, affected upper-flow regime conditions, depositing at the lee-side of the bar influenced by lower- flow regime conditions. Temporal flow variabilities are mostly discernible through fluvial architectural analysis, by evidence of flow pulsations, and recognition of low- and high- discharge channels.

The WWL records persistent shallow water-table, and ephemeral sheet-floods, which reduced the availability of dry sands to be transported by the wind, inhibiting the accumulation of aeolian dunes, resulting in the dominance of hybrid sand sheets. Periods of water-table lowering, are first recorded by sand-drift surfaces and blowout hollows, followed by wind saturation with sand, and deposition of aeolian dunes. Thus, the hybrid sand sheets and the aeolian dunes took place in distinct temporal moments. Distal parts of the LGV record an increase in the frequency of WWL occurrences, and a decrease in the number of larger fluvial cross-sets. These characteristics, coupled with discharge variabilities, aggradation, and the extensive coverage of the Middle Buntsandstein fluvial deposits, support a hypothesis that the LGV was part of a large distributive fluvial system (fan/megafan). However, a larger-scale quantitative analysis is necessary for a conclusive characterisation.

Previous authors have interpreted the base of WWL, marked by sand-drift surfaces, as formed during climatic changes that can be correlated across the German Basin. However, ambiguity is highlighted, once evidence indicates that WWL and FC may be contemporaneous, and their establishment be associated with channel-belt avulsion events. Therefore, understanding the events responsible for the development of these surfaces is crucial before laterally extrapolating them for several kilometres, since in some cases, their lateral extension cannot be followed even at an outcrop scale (hundreds of metres).

ACKNOWLEDGEMENTS

This study is part of Lucas M. Bofill's PhD project, funded by the École Doctorale des Sciences de la Terre et de l'Environnement (ED413), and by the Interdisciplinary Thematic Institute Geosciences for the energy system transition, as part of the ITI 2021-

2028 program of the University of Strasbourg, CNRS and Inserm, supported by Idex Unistra (ANR-10-IDEX-0002), and by SFRI-STRAT'US project (ANR-20-SFRI-0012). We acknowledge ES-Géothermie, more specifically Albert Genter, Carole Glass, and Eleonore Dalmais for providing the access and structure to describe the core EPS1. We also thank Professor Nigel Mountney and an anonymous reviewer, for their time and effort invested, providing great contribution to this manuscript. Last but not least, special thanks to those who enriched the content and discussions of this study: Adriano Reis, Felipe Guadagnin, Gabriela Knobelock, Laura Menezes, Laurent Gindre, Philippe Ackerer, Philippe Duringer, and Renato Paes de Almeida.

REFERENCES

Aichholzer, C., 2019. Le log complet de la stratigraphie de la zone rhénane ainsi que les modalités stratigraphiques, sédimentaires et structurales de la transition « socle-couverture ». Aplication a la géothermie profonde. PhD thesis. Université de Strasbourg. École doctorale des Sciences de la Terre et de l'Environnement (ED413), Intitut de Physique du Globe de Strasbourg (UMR7516). 546 p. (In French).

Akoglu, H., 2018. User's guide to correlation coefficients. Turkish Journal of Emergency Medicine, 18, 91-93.

Al-Masrahy, M.A. and Mountney, N.P., 2013. Remote sensing of spatial variability in aeolian dune and interdune morphology n the Rub' Al-Khali, Saudi Arabia. Aeolian Research. 11, 155-170.

Al-Masrahy, M.A. and Mountney, N.P., 2015. A classification scheme for fluvial-aeolian system interaction in desert-margin settings. Aeolian Research. 17, 67-88.

Alexander, J., Bridge, J.S., Cheel, R.J., Leclair, S.F., 2001. Bedforms and associated sedimentary structures formed under supercritical water flows over aggrading sand beds. Sedimentology. 48, 133-152.

Alexander, J., Herbert, C.M., Fielding, C.R., Amos, K.J., 2020. Controls on channel deposits of highly variable rivers: comparing hydrology and event deposits in the Burdekin River, Australia. Sedimentology. 67, 2721-2746.

Allen, J.R.L. and Leeder, M.R., 1980. Criteria for the instability of upper-stage plane beds: Sedimentology. 27, p. 209–217. doi:10.1111/j.1365-3091.1980.tb01171.x.

Allen, J.R.L., 1983a. Studies in fluviatile sedimentation: bars, bars-complexes and sandstone sheets (Low sinuosity braided streams) in the Brownstones (L/ Devonian), Welsh Borders, Sedimentary Geology. 33, 237-239.

Allen, J.R.L., 1983b. Gravel overpassing on humpback bars supplied with mixed sediment: examples from the Lower Old Red Sandstone, southern Britain. Sedimentology. 30, 285-294.

Allmendinger, R. W., Cardozo, N., AND Fisher, D., 2012. Structural geology algorithms: Vectors and tensors in structural geology: Cambridge University Press.

Arévalo, O.J., Colombera, L., Mountney, N.P., Basilici, G., Soares, M.V.T., 2022. Variations in water discharge at different temporal scales in a mud-prone alluvial succession: The Paleocene-Eocene of the Tremp-Graus Basin, Spain. Sedimentary Geology. 433, 24 p. https://doi.org/10.1016/j.sedgeo.2022.106122

Aquilina, L., Pauwels, Genter, A., Fouillac, C., 1997. Water-rock interaction processes in the Triassic sandstone and the granitic basement of the Rhine Graben: Geochemical investigation of a geothermal reservoir. Geochimica et Cosmochimica Acta. 61, N° 20, 4281-4295.

Banks E.W., Morgan, L.K., Loui, A.J.S., Dempsey, D., Wilson, S.R., 2022. Active distributed temperature sensing to assess surface water-groundwater interaction and river loss in braided river systems. Journal of Hydrology. 615, 12 p. https://doi.org/10.1016/j.jhydrol.2022.128667

Basilici, G, Mesquita, A.F., Soares, M.V.T.S., Janočko, J., Mountney, N.P., Colombera, L., 2021. A Mesoproterozoic hybrid dry-wet aeolian system: Galho do Miguel Formation, SE Brazil. Precambrian Research. 359, 23 p.

Belle, G.V., Martin, D.C., 1993. Sample size as a function of Coefficient of Variation and Ration of Means. The American Statistician. 43, N°3, 165-167.

Bhattacharyya, A., Morad, S., 1993. Proterozoic braided ephemeral fluvial deposits: an example from the Dhandraul Sandstone Formation of the Kaimur Group, Son Valley, central India. Sedimentary Geology. 84, 101-114.

Botsch, R.E., 2011. Chapter 12. Significance and Measures of Association. Political Science Program. Aiken University of South Carolina. Accessed on July 26th, 2023. https://polisci.usca.edu/apls301/Text/Chapter%2012.%20Significance%20and%20M eas ures%20of%20Association.htm

Bouly, S., Demassieux, L., 1996. Structure, caractéristiques et fonctionnement du réservoir aquifère des Grès Inférieurs du Trias en Lorraine. La houille blanche/N° 76.

Bourquin, S. and Durand, M., 2006. International field workshop on “The Triassic of Eastern France”, October 2-7, 2006. HAL archives-ouvertes.fr. 81p.

Bourquin, S., Peron, S., Durand, M., 2006. Lower Triassic sequence stratigraphy of the western part of the Germanic Basin (west of Black Forest): Fluvial system evolution through time and space. Sedimentary Geology. 186, 187 – 211.

Bourquin, S., Guillocheau, F., Peron, S., 2009. Braided rivers within an arid alluvial plain (example from the Lower Triassic, western German Basin): recognition criteria and expression of stratigraphic cycles. Sedimentology. 56, p. 2235 – 2264. doi: 10.1111/j.1365-3091.2009.01078.x

Bridge, J.S., 2003, Rivers and Floodplains: Oxford, U.K., Blackwell, 491 p.

Bristow C. and Mountney N.P., 2013. Aeolian Stratigraphy. In: SHRODER, J.F., 2013. Treatise on Geomorphology. 11, p. 246-268. San Diego: Academic Press.

Brookfield, M.E., 2008. Palaeoenvironments and palaeotectonics of the arid to hyperarid intracontinental latest Permian- late Triassic Solway basin (U.K.). Sedimentary Geology. 210, 27-47.

Cain, S.A. and Mountney, N.P., 2009. Spatial and temporal evolution of a terminal fluvial fan system: the Permian Organ Rock Formation, South-east Utah, USA. Sedimentology. 56. 1774-1800. Doi: 10.1111/j.1365-3091.2009.01057.x

Carr-Crabaugh, M. and Kocurek, G., 1993. Entrada Sandstone: and exemple of a wet aeolian system. In: The Dynamics and Environmental Context of Aeolian Sedimentary Systems. Geological Society London Special Publication. 72, 103-126.

Carr-Crabaugh, M. and Kocurek, G., 1998. Continental sequence stratigraphy of a wet eolian system: a key to relative sea-level change. Relative Role of Eustasy, Climate, and Tectonismo in Continental Rocks, SEPM Special Publication. 59, 17 p.

Cardozo, N., and Allmendinger, R.W., 2013. Spherical projections with OSXStereonet. Computers and Geosciences, 51, 193 – 205. doi:10.1016/ j.cageo.2012.07.021.

Carling, P.A., 1990. Particle over-passing on depth-limited gravel bars. Sedimentology. 37, p. 345-355.

Clemmensen, L.B., Abrahamsen, K., 1983. Aeolian stratification and facies association in desert sediments, Arran basin (Permian), Scotland. Sedimentology. 30, 311-339.

Clemmensen, L.B., Tirsgaard, H., 1990. Sand-drift surfaces: A neglected type of bounding surface. Geology. 18, 1142 – 1145.

Clemmensen, L.B. , 1991. Controls on aeolian sand sheet formation exemplified by the Lower Triassic of Helgoland. Acta Mechanica, 2: 161-170.

Collinson, J.D., 1996. Alluvial Sediments. Chapter 3 in: Sedimentary Environments: Processes, Facies and Stratigraphy. 3rd edition.

Collinson, J.D., Mountney, N., Thompson, D., 2006. Sedimentary structures. 3rd Edition. Terra Publishing, England, 292 p.

Colombera, L., Mountney, N.P., McCaffrey, W.D., 2013. A quantitative approach to fluvial facies models: Methods and example results. Sedimentology. 60(6). 1526-1558. https://doi.org/10.1111/sed.12050

Colombera, L., Mountney, N.P., 2019. The lithofacies organization of fluvial channel deposits: A meta-analysis of modern rivers. Sedimentary Geology. 383, 16-40. https://doi.org/10.1016/j.sedgeo.2019.01.011

Colombera, L., Reesink, A.J.H., Duller, R.A., Jeavons, V.A., Mountney, N.P., 2024. The thickness variability of fluvial cross-strata as a record of dune disequilibrium and palaeohydrology proxy: A test against channel deposits. Sedimentology. 71, 590-618.. doi: 10.1111/sed.13147

Cosgrove, G.I.E., Colombera, L., Mountney, N.P., 2022. The role of subsidence and accommodation generation in controlling the nature of the aeolian stratigraphic record. Journal of the Geological Society. 179, 23 p. https://doi.org/10.6084/m9.figshare.c.5515695.v1

Cowan, G., 1993. Identification and significance of aeolian deposits within the dominantly fluvial Sherwood Sandstone Group of the East Irish Sea Basin UK. In: NORTH, C.P. and PROSSER, D.J., 1993. Characterization of Fluvial and Aeolian Reservoirs. Geological Society Special Publication. No 73, 231-245.

Dachroth, W., 1985. Fluvial sedimentary styles and Associated Depositional Environments in the Buntsandstein Wes of River Rhine in Saar Area and Pfalz (F.R. Germany) and Vosges (France). In: Mader, D., Aspects of fluvial sedimentation in the Lower Triassic Buntsandstein of Europe. Lecture notes in Earth Sciences. 4: 197-248, Berlin/Heidelberg / New York / Tokio (Springer).

Davidson, S.K., Hartley, A.J., Weissmann, G.S., Nichols, G.J., Scuderi, L.A., 2013. Geomorphic elements on modern distributive fluvial systems. Geomorphology. 180-181, 82-95. http://dx.doi.org/10.1016/j.geomorph.2012.09.008

Davis, J.C., 2002. Statistics and Data Analysis in Geology, Third Edition: John Wiley and Sons, 638 p.

DeLuca, J.L. and Eriksson, K.A., 1989. Controls on synchronous ephemeral- and perennial-river sedimentation in the middle sandstone member of the Triassic Chinle Formation, northeastern New Mexico, U.S.A. Sedimentary Geology. 61, 155-175.

Deynoux, M., Duringer, P., Gall, J.C., Grauvogel-Stamm, L., Simon, G., 1997. Permian and Triassic of the northern Vosges mountains. Field trip guide book -18th European Regional Meeting of Sedimentology, Heidelberg, September 2-4. 11 p.

Dixon, J.C., 2014. Lag Deposit. In: Encyclopedia of Planetary Landforms. Springer, New York, NY. https://doi.org/10.1007/978-1-4614-9213-9_214-1

Duller, R.A., Mountney, N.P., Russell, A.J., Cassidy, N.C., 2008. Architectural analysis of a volcaniclastic jökulhlaup deposit, southern Iceland: sedimentary evidence for supercritical flow. Sedimentology. 55, 939–964.

Durand, M., 1978. Paléocourants et reconstituition paléogeographique: l'exemple du Buntsandstein dans les Vosges Méridionales, Thesis, Université de Nancy-I. (In French).

Durand, M., Bourquin, S., 2013. Criteria for the identification of ventifacts in the geological record: A review and new insights. Comptes Rendus Geoscience. 35, 111- 125.

Duringer, P., Aichholzer, C., Orciani, S., Genter, A., 2019. The complete lithostratigraphic section of the geothermal wells in Rittershoffen (Upper Rhine Graben, eastern France): a key for future geothermal wells. BSGF – Earth Sciences Bulletin 2019, Vol, 190008. Avaliable at www.bsgf.fr.

Ethridge, E.G., Skelly, R.L., Bristow, C.S., 1999. Avulsion and crevassing in the sandy, braided Niobrara River: complex response to base-level rise and aggradation. Fluvial sedimentology - Special Publication International Association of Sedimentologists. 28, 179-191. IBSN: 978-0-632-05354-4.

Farraj, A.A., Harvey, A.M., 2004. Late Quaternary interactions between aeolian and fluvial processes: a case study in the northern UAE. Journal of Arid Environments. 56, 235-248.

Fielding, C.R., 2006. Upper flow regime sheets, lenses and scour fills: Extending the range of architectural elements for fluvial sediment bodies. Sedimentary Geology. 170:1-4, p. 227-240. doi: 10.1016/j.sedgeo.2006.05.009

Fielding, C.R., Allen, J.P., Alexander, J., Gibling, M.R., 2009. Facies model for fluvial systems in the seasonal tropics and subtropics. Geology. 37, n°7, 623-626. doi: 10.1130/G25727A.1

Fielding, C.R., Ashworth, P.J., Best, J.L., Prokocki, E.W., Smith, G.H.S., 2012. Tributary, distributary and other fluvial patterns: What really represents the norm in the continental rock record? Sedimentary Geology. 261-262, 15-32. doi:10.1016/j.sedgeo.2012.03.004

Fielding, C.R., Alexander, J., Allen, J.P., 2018. The role of discharge variability in the formation and preservation of alluvial sediment bodies. Sedimentary Geology. v.365, 1- 20.

Folk, R.L., Andrews, P.B., Lewis, D.W., 1970. Detrital sedimentary rock classification and nomenclature for use in New Zeland. New Zealand Journal of Geology and Geophysics. 13, 937-968. http://dx.doi.org/10.1080/00288306.1970.10418211

Fries, D., Lebouil, S., Maurer, V., Martin, C., Baujard, C., Ravier, G., Bobuais, R., Amari, S., 2022. Lithium extraction through pilot scale test under real geothermal conditions of the Upper Rhine Graben. European Geothermal Congress, 2022. Berlin, Germany, 17 – 21 October, 2022. 8 p.

Fryberger, S.G., Schenk, C.J., 1988. Pin stripe lamination: a distinctive feature of modern and ancient eolian sediments. Sedimentary Geology. 55. 1-15.

Fryberger, S.G., Schenk, C.J., Krystink, 1988. Stokes surfaces and the effects of near surface groundwater-table on aeolian deposition. Sedimentology. 35, 21-41.

Fryberger, S.G., 1991. A review of aeolian bounding surfaces, with examples from the Permian Minnelusa Formation, USA. In: North, C.P. & Prosser, D.J., 1993, Characterization of Fluvial and Aeolian Reservoirs, Geological Society Special Publication, No 73, 167-197.

Fryberger, S. G., Hesp, P., Hastings, K., 1992. Aeolian granule ripple deposits, Namibia. Sedimentology. 39, 319–331. doi:10.1111/j.1365-3091.1992.tb01041.x

Galeazzi, C.P., Almeida, R.P., Prado, A.H., 2021. Linking rivers to the rock record: Channel patterns and paleocurrent circular variance. Geology. p. 1402-1407. https://doi.org/10.1130/G49121.1

Gall J., 1972. Permanence du régime de chenaux et de flaques dans les Vosges du Nord pendant toute la durée du Buntsandstein. In: Sciences Géologiques. Bulletin,

tome 25, n°4, 1972. Sédimentologie et géochimie de la surface. 307- 322. (In French).

Gall, J., Durand, M., Muller, E., 1977. Le Trias de part et d'autre du Rhin. Corrélations entre les marges et le centre du bassin germanique. Bulletin du B.R.G.M. (deuxième série). Section IV, n°3 – 1977, 193-204. (In French).

Gérard, A., Genter, A., Kohl, T., Lutz, P., Rose, P., Rummel, F., 2006. The deep EGS (Enhanced Geothermal System) project at Soultz-sous-Forêts (Alsace, France). Geothermics. 35, 473-483.

Gerdes, G., 2007. Structures left by modern microbial mats in their host sediments. Chapter 2 In: Atlas of microbial mat features preserved within the clastic rock record, Shieber, J., Bose, P.K., Eriksson, P.G., Banerjee, S., Sarkar, S., Altermann, W., and Catuneanu, O., Elsevier, 5-38.

Ghienne, J.F, Deynoux, M, Jeannetter, D., 1994. Structures sédimentaires, discontinuités et caractères pétrophysiques des grès du Buntsandstein des Vosges du Nord, Trias de l'Est de la France. C.R. Acad. Sci. Paris, t. 319, série II, 1351 - 1358. (In French, abstract in English).

Ghienne, J.F, Girard, F., Moreau, J., Rubino, J.L., 2010. Late Ordovician climbing-dune cross-stratification: a signature of outburst floods in proglacial outwash environments? Sedimentology. 57, 1175-1198. doi: 10.1111/j.1365-3091.2009.01142.x

Ghinassi, M., Magi, M., Sagri, M., Singer, B.S., 2004. Arid climate 2.5 Ma in the Plio-Pleistocene Valdrano Basin (Northern Apennines, Italy). Paleogeography, Paleoclimatology, Paleoecology. 207, 37-57. doi:10.1016/j.palaeo.2004.01.020

Grimmer, J.C., Ritter, J.R.R., Eisbacher, G.H., Fielitz, W., 2017. The Late Variscan control on the location and asymmetry of the Upper Rhine Graben. International Journal of Earth Sciences. 106, 827-853.

Gross, E.C., Carr, M., Jobe, Z.R., 2022. Three-dimensional bounding surface architecture and lateral facies heterogeneiry of a wet aeolian system: Entrada Sandstone, Utah. Sedimentology. 70, 145-178.

Guillocheau, F., Robin, C., Allemand, P., Bourquin, S., Brault, N., Dromart, G., Friedenberg, R., Garcia, J.P., Gaulier, J.M., Gaumet, F., Grosdoy, B., Hanot, F., Le Strat, P., Mettraux, M., Nalpas, T., Prijac, C., Rigollet, C., Serrano, O., Grandjean, G., 2000. Meso-Cenozoic geodynamic evolution of the Paris Basin: 3D stratigraphic constraints. Geodin. Acta. 13, 189–246

Hajek, E.A., Heller, P.L., Sheets, B.A., 2010. Significance of channel-belt clustering in alluvial basins. Geology. 38, n°6, 535-538. doi: 10.1130/G30783.1

Hansford, M.R., Plink-Björklund, P., 2020. River discharge variability as the link between climate and fluvial fan formation. Geology. 5 p. https://doi.org/10.1130/G47471.1

Hartley, A.J., Weissmann, G.S., Nichols, G.J., Warwick, G.L., 2010. Large distributary fluvial systems: characteristics, distribution, and controls on development. Journal of Sedimentary Research. 80, 167-183. DOI: 10.2110/jsr.2010.016

Hartley, A.J., Owen, A., 2022. Paleohydraulic analysis of an ancient distributive fluvial system. Journal of Sedimentary Research. v.92, 445-459. DOI: 10.2110/jsr.2021.062

Havholm, K.G. and Kocurek, G., 1994. Factors controlling aeolian sequence stratigrapgy: clues from super bounding surface features in the Middle Jurassic Page Sandstone. Sedimentology. 41, 913-934.

Herivaux, C., Marechal, J., 2019. Prise en compte des services dépendants des aquifères dans les démarches d'évaluation des services écosystémiques. Rapport final, BRGM/RP-68929-FR. 107 p. (In French).

Hesp, P.A., Walker, I.J., 2013. Coastal dunes. In: Shroder, J., Lancaster, N., Sherman, D.J.; Baas, A.C.W., 2013. Treatise on Geomorphology. Academic Press, San Diego, CA, 11. Aeolian Geomorphology, 328-355.

Hjellbakk, A., 1997. Facies and fluvial architecture of a high-energy braided river: the Upper Proterozoic Segglodden Member, Varanger Peninsula, northern Norway. Sedimentary Geology. 131-161.

Høimyr, Ø., Kleppe, A., Nystuen, J.P., 1992. Effects of heterogeneities in a braided stream channel sandbody on the simulation of oil recovery: a case study from the Lower Jurassic Statfjord Formation, Snorre Field, North Sea. In: Ashton, M., Advances in Reservoir Geology. Geological Society of London, Special Publication. 69, 105–134

Hunter, R.E., 1977. Basic types of stratification in small eolian dunes. Sedimentology. 24, 361-387.

Jones, L.S. and Blakey, R.C., 1997. Eolian-fluvial interaction in the Page Sandstone (Middle Jurassic) in south-central Utah, USA – a case study of erg-margin processes. Sedimentary Geology. 109, 181-198.

Kendall, M. G., 1938. A New Measure of Rank Correlation, Biometrika, 30, 81-93.

Kifumbi, C., Scherer, C.M.S., Michel, R.D.L., Reis, A.D., Guadagnin, F., Souza, E.G., Ferronato, J.P.F., JONES, F.H., 2023. Spatial and temporal variation in the evolution of ancient aeolian dune-field. The Pennsylvanian Piaui Formation (Parnaiba Basin), Brazil. Sedimentary Geology. 451. https://doi.org/10.1016/j.sedgeo.2023.106398

Kocurek, G. and Fielder, G., 1982. Adhesion structures. Journal of Sedimentary Petrology. 2. No. 4, 1229-1241.

Kocurek, G. and Nielson, J., 1986. Conditions favourable for the formation of warm climate sand seas. Sedimentology. 33, 795-816.

Kocurek, G., 1988. First-order and super bounding surfaces in eolian sequences – Bounding surfaces revisited. Sedimentary Geology. 56, 193-206.

Kocurek, G., 1991. Interpretation of ancient eolian sand dunes. Annu. Rev. Earth Planet. Sci. 19, 43-75.

Kölbel, T, Genter, A., 2017. Enhanced geothermal systems: the Soultz-sous-Forêts project, 243–248. In: UYAR, T.S., 2017. Towards 100% Renewable Energy: Techniques, Costs and Regional Case-Studies. https://doi.org/ 10.1007/978-3-319-45659-1_25

Kölbel, L., Kölbel, T., Sauter, M., Schäfer, T., Siefert, D., 2020. Identification of fracture zones in geothermal reservoirs in sedimentary basins: A radionuclide-based approach. Geothermics. 85, 10 p.

Kukulski, R.B., Hubbard, S.M., Moslow, T.F., Raines, M.K., 2013. Basin-scale stratigraphic architecture of upstream fluvial deposits: Jurassic-Cretaceous foredeep, Alberta basin, Canada. Journal of Sedimentary Research. 83, 704-722. DOI: 10.2110/jsr.2013.53

Lane, T.I., Nanson, R.A., Ainsworth, R.B., Vakarelov, B.K., 2023. The Holocene Mitchell Megafan, Gulf of Carpentaria, Australia. Chapter 12 in: Wilkinson, M.J. and Gunnell, Y., 2023. Fluvial Megafans on Earth and Mars. https://doi.org/10.1017/9781108525923

Lang, J., Le Heron, D.P, Berg, J.V.D., Winsemann, 2021. Bedforms and sedimentary structures related to supercritical flows in glaciogenic settings. Sedimentology. 68, 1539 – 1579. doi: 10.1111/sed.12776

Langford, R.P., 1989. Fluvial-aeolian interactions: Part I, modern systems. Sedimentology. 36, 1023-1035.

Leary, K.C.P., Ganti, V., 2019. Preserved Fluvial Cross Strata Record Bedform Disequilibrium Dynamics. Geophysical Research Letters. 47, 11 p. https://doi.org/ 10.1029/2019GL085910

Leclair, S.F., Brigde, J.S., 2001. Quantitative interpretation of sedimentary structures formed by river dunes. Journal of Sedimentary Research. 71, N 5, 713-716.

Leier, A.L., Decelles, P.G., Pelletier, J.D, 2005. Mountains, monsoons and megafans. Geology. 33, 289-292. https://doi.org/10.1130/G21228.1

Leleu, S., Hartley, A.J., Williams, B.P.J., 2009. Large-scale alluvial architecture and correlation in a Triassic pebbly braided river system, Lower Wolfville Formation (Fundy basin, Nova Scotia, Canada). Journal of Sedimentary Research. 79, 265-286. DOI: 10.2110/jsr.2009.034

Li, S., Yu, X, Chen, B., Li, S., 2015. Quantitative characterization of architecture elements and their response to base-level change in a sandy braided fluvial system

at a mountain front. Journal of Sedimentary Research. 85, 1285-1274. DOI: http://dx.doi.org/10.2110/jsr.2015.82.

Li, W., ColomberA, L., Yue, D., Mountney, N., 2022. Controls on the morphology of braided rivers and braided bars: An empirical characterization of numerical models. Sedimentology. 21 p. doi: 10.1111/sed.13040

Liu, K., Boult, P., Painter, S., Paterson, L., 1996. Outcrop analog for sandy braided stream reservoirs: Permeability patterns in the Triassic Hawkesbury Sandstone, Sydney Basin, Australia. AAPG Bulletin. 80, 1850-1866.

Lyster, S.J., Whittaker, A.C., Hajek, E.A., Ganti, V., 2022. Field evidence for disequilibrium dynamics in preserved fluvial cross-strata: A record of discharge variability of morphodynamic hierarchy? Earth and Planetary Sciences Letters. 579. 12p. https://doi.org/10.1016/j.epsl.2021.117355

Mader, D., 1985. Aspects of fluvial sedimentation in the Lower Triassic Buntsandstein of Europe. Lecture notes in earth sciences. 634 p.

Manna, M.O., Scherer, C.M.S., Bállico, M.B., Reis, A.D., Moraes, L.V., Ferrari, L.A.B., Roisenberg, H.B., Oliveira, V.G., 2021. Changes in fluvial architecture induced by discharge variability, Jaicós Formation (Silurian-Devonian), Parnaíba Basin, Brazil. Sedimentary Geology, 420, 23 p. https://doi.org/10.1016/j.sedgeo.2021.105924.

McKie, T., 2011. Architecture and behavior of dryland fluvial reservoirs, Triassic Skagerrak Formation, Central North Sea. In: Davidson, S.K., Leleu, S., North, C.P. (Eds.), From River to Rock Record: The Preservation of Fluvial Sediments and their Subsequent Interpretation. 97. SEPM Special Publication, 189–214.

McLeod, J.S., Wood, J., Lyster, S.J, Valenza, J.M., Spencer, A.R.T, Whittaker, A.C., 2023. Quantitative constraints on flood variability in the rock record. Nature Communications. 14:3362. 12 p. https://doi.org/10.1038/s41467-023-38967-8.

Medici, G., Boulesteix, K., Mountney, N.P., West, L.J., Odling, N.E., 2015. Palaeoenvironmental of braided fluvial systems in different tectonic realms of the Triassic Sherwood Sandstone Group, UK. Sedimentary Geology. 329, 188-210. http://dx.doi.org/10.1016/j.sedgeo.2015.09.012

Miall, A.D., 1977. A review of the braided-river depositional environment. Earth Sci. Rev. 13, 1–62.

Miall, A.D., 1985. Architectural-element analysis: a new method of facies analysis applied to fluvial deposits. Earth-Sci. Rev. 22, 261-308.

Miall, A.D., 1988. Architectural elements and bounding surfaces in fluvial deposits: anatomy of the Kayenta formation (Lower Jurassic), Southwest Colorado. Sedimentary Geology. 55, 233-262.

Miall, A.D., 2006. The Geology of Fluvial Deposits: Sedimentary Facies, Basin Analysis and Petroleum Geology. 4th edition. 599 p.

Myrow, P.M., Jerolmack, D.J., Perron, J.T., 2018. Bedform disequilibrium. Journal of Sedimentary research. 88, 1096–1113.

Mountney, N., Howell, J., Flint, S., Jerram, D., 1999. Climate, sediment supply and tectonics as controls on the deposition and preservation of the aeolian-fluvial Etjo Sandstone Formation, Namibia. Journal of the Geological Society. 156, 771-777.

Newell, A.J., 2001. Bounding surfaces in a mixed aeolian-fluvial system (Rotliegend, Wesses Basin, SW UK). Marine and Petroleum Geology. 18, 339-347.

Núñez-González, F., and Martín-Vide, 2010. Downstream-migrating antidunes in sand, gravel and sand-gravel mixtures. River Flow, Dittrich, Koll, Aberle & Geisenhainer (eds). 8 p.

Ohata, K., Naruse, H., Izumi, N., 2022. Upper and lower plane bed definitions revised. Progress in Earth and Planetary Science. 9:23. 13 p. https://doi.org/10.1186/s40645- 022-00481-8

Paola, C., Borgman, L., 1991. Reconstructing random topography from preserved stratification. Sedimentology. 38, 553-565.

Paim, P.S.G. and Scherer, C.M.S., 2007. High-resolution stratigraphy and depositional model of wind- and water-laid deposits in the ordovician Guaritas rift (Southernmost Brazil). Sedimentary Geology. 202, 776-795. doi:10.1016/j.sedgeo.2007.09.003

Perriaux, J., 1961. Contribuition à la géologie des Vosges gréseuses. Strasbourg: Service de la carte géologique d'Alsace et de Lorraine. 1-236. (In French).

Plink-Björklund, P., 2015. Morphodynamics of rivers strongly affected by monsoon precipitation: Review of depositional style and forcing factors. Sedimentary Geology. 323, 110-147. http://dx.doi.org/10.1016/j.sedgeo.2015.04.004

Porter, M.L.,1987. Sedimentology of an ancient erg margin: the Lower Jurassic Aztec Sandstone, southern Nevada and southern California. Sedimentology, 34, 661- 680.

Priddy, C.L., Clark, S.M., 2021. Spatial variation in the sedimentary architecture of a dryland fluvial system. Sedimentology. 68. 2887-2917.

Reesink, A.J.H, Van Den Berg, J.H., Parsons, D.R ., Amsler, M.L., Best, J.L., Hardy, R.J., Orfeo, O., Szupiany, R.N., 2015. Extremes in dune preservation: Controls on the completeness of fluvial deposits. Earth-Science Reviews. 150, 652-665. http://dx.doi.org/10.1016/j.earscirev.2015.09.008

Reis, A.D., Scherer, C.M.S., Owen, A., Amarante, F.B., Ferronato, J.P.F., Pantopoulos, G., Souza, E.G., Ballico, M.B., Aguilar, C.A.G., 2022. A quantitative depositional model of a large distributive fluvial system (megafan) with terminal

aeolian interactions: the Upper Jurassic Guará DFS in southwestern Gondwana. Journal of Sedimentary Research. 92, 460-485. DOI: 10.2110/jsr.2021.040

Rittner, M., Vermeesch, P., Carter, A., Bird, A., Stevens, T., Garzanti, E., Vezzoli, G., Dutt, R., Xu, Z., Lu, H., 2016. The provenance of Taklamakan desert sand. Earth and Planetary Science Letters. 437, 127–137.

Rodríguez-López, J.P., Clemmensen, L.B., Lancaster, N., Mountey, N.P., Veiga, G.D., 2014. Archean to Recent aeolian sand systems and their sedimentary record: Current understanding and future prospects. Sedimentology. 61, 1487-1534.

Røe, S., 1987. Cross-strata and bedforms of probable transitional dune to upper-stage plane-bed origin from a Late Precambrian fluvial sandstone, northern Norway. Sedimentology. 34, 89-101.

Rossi, C., Kälin, O., Arribas, J., Tortosa, A., 2002. Diagenesis, provenance and reservoir quality of Triassic TAGI sandstones from Ourhoud field, Berkine (Ghadames) Basin, Algeria. Marine and Petroleum Geology. 19, 117–142.

Steel, R.J., Thompson, D.B., 1983. Structures and textures in Triassic braided stream conglomerates (‘Bunter’ Pebble Beds) in the Sherwood Sandstone Group, North Staffordshire, England. Sedimentology. 30, 341-367.

Théobald, N., Perriaux, J., Langenfeld, F., Both, J., 1967. Carte géologique 1/50000 Bitche- Walschbronn XXXVIII3. (In French).

Sambrook Smith, G.H., Best, J.L., Ashworth, P.J., Fielding, C.R., Goodbred, S.L., Prokocki, E.W., 2010. Fluvial form in modern continental sedimentary basins: distributive fluvial systems: Comment. Geol. Forum. 38, e230. http://dx.doi.org/10.1130/G31507C.1

Sanjuan, B., Gourcerol, B., Millot, R., Rettenmaier, D., Jeandel, E., Rombaut, A., 2022. Lithium-rich brines in Europe: An up-date about geochemical characteristics and implications for potential Li resources. Geothermics. 101, 18 p.

Sauderson, H.C., Lockett, F.P.J., 1983. Flume Experiments on bedforms and structures at the dune-plane bed transition. Special Publications International Association of Sedimetologists. 6, 49-58.

Sharma, N., Whittaker, A.C., Watkins, S.E., Valero, L., Verite, J., Puigdefabregas, C., Adatte, T., Garces, M., Guillocheau, F., Castelltort, S., 2023. Water discharge variations control fluvial stratigraphic architecture in the Middle Eocene Escanilla formation, Spain. Nature Scientific Reports. 15 p. https://doi.org/10.1038/s41598-023-33600-6

Scherer, C.M.S., 2000. Eolian dunes of the Botucatu Formation (Cretaceous) in southernmost Brazil: morphology and origin. Sedimentary Geology. 137, 63-84. https://doi.org/10.1016/S0037-0738(00)00135-4.

Scherer, C.M.S. and Lavina, E.L.C., 2005. Sedimentary cycles and facies architecture of aeolian-fluvial strata of the Upper Jurassic Guará Formation, southern Brazil. Sedimentology. 52, 1323-1341. doi: 10.1111/j.1365-3091.2005.00746.x

Scherer, C.M.S., Goldberg, K., Bardola, T., 2015. Facies architecture and sequence stratigraphy of an early post-rift fluvial succession, Aptian Barbalha Formation, Araripe Basin, northeastern Brazil. Sedimentary Geology. 322, 43-62. http://dx.doi.org/10.1016/j.sedgeo.2015.03.010.

Skelly, R.L., Bristow, C.S., Ethridge, F.G., 2003. Architecture of channel-belt deposits in an aggrading shallow sandbed braided river: the lower Niobrara River, northeast Nebraska. Sedimentary Geology. 158. 249-270. doi:10.1016/S0037-0738(02)00313-5

Southard, J.B., 1991. Experimental determination of bed-form stability. Annual Review of Earth and Planetary Sciences. 19(1), 423-455. DOI: 10.1146/annurev.ea.19.050191.002231

Trewin, N., 1993. Mixed aeolian sandsheet and fluvial deposits in the Tumblagooda Sandstone, Western Australia. In: NORTH, C.P. and PROSSER, D.J. (eds), 1993, Characterization of Fluvial and Aeolian Reservoirs. Geological Society Special Publications. No 73, 219-230.

Walker, R.G., 1992. Facies, facies models and modern stratigraphic concepts. In: Walker, R.G., James, N.P. (Eds.), Facies Models - in Response to Sea Level Change, 1–14.

Walker, S., Holbrook, J., 2023. Structures, architecture, vertical profiles, paleohydrology and taphonomy of an upper-flow-regime-dominated fluvial system, the Triassic Dockum Group of the Palo Duro Canyon, Texas. Sedimentology. 70, 645-684. doi: 10.1111/sed.13041.

Wang, J., Plink-Björklund, P., 2019. Stratigraphic complexity in fluvial fans: Lower Eocene Green River Formation, Uinta Basin, USA. Basin Research. 31, 892-919. https://doi.org/10.1111/bre.12350

Weissmann, G.S., Hartley, A.J., Nichols, G.J., Scuderi, L.A., Olson, M., Buehler, H., Banteah, R., 2010. Fluvial form in modern continental sedimentary basins: distributive fluvial systems. Geology. 38, 39–42.

Weissmann, G.S., Hartley, A.J, Scuderi, L.A., NIchols, G.J., Owen, A., Wright, S., Felicia, A.L., Holland, F., Anaya, F.M.L., 2015. Fluvial geomorphic elements in modern sedimentary basins and their potential preservation in the rock record: A review. Geomorphology. 205, 187-219. https://doi.org/10.1016/j.geomorph.2015.09.005

Wilkinson, J.M., Gunnel, Y., 2023. Megafans as Major Continental Landforms. Chapter 1 in: Wilkinson, M.J. and Gunnell, Y., 2023. Fluvial Megafans on Earth and Mars. https://doi.org/10.1017/9781108525923.

Wizevich, M.C., 1992. Sedimentology of Pennsylvanian quartzose sandstones of the Lee Formation, central Appalachian Basin: fluvial interpretation based on lateral profile analysis. Sedimentary Geology. 78, 1–47.

Vaute, L., Gigleux, S., Ngyen-The, 2007. Eaux souterraines du départment des Vosges: Caractérisation des principals ressources exploitables et revision du modèle de gestion de la nappe des grés du Trias inférieur. Rapport final, BRGM/RP-55653-FR. 396 p. (In French).

Vaute, L., Innocent, C., Fourniguet, 2013. Actualisation du modèle hydrogeologique de la nappes des grès du Trias en Lorraine. Rapport final. BRGM/RP-62405-FR. 60p. (In French).

Veiga, G.D., Spalletti, L.A., Flint, S., 2002. Aeolian/Fluvial interaction and high-resolution sequence stratigraphy of a non-marine lowstand wedge: the Avilé Member of the Agrio Formation (Lower Cretaceous), central Neuquén Basin, Argentina. Sedimentology. 49, 1001-1019. DOI: 10.1046/j.1365-3091.2002.00487.x

Ventra, D. and Moscariello, A., 2023. Geology of Fluvial-Fan Deposits: Facies Patterns, Architectural Organisation and Implications for Economic Geology. Chapter 14 in: Wilkinson, M.J. and Gunnell, Y., 2023. Fluvial Megafans on Earth and Mars. https://doi.org/10.1017/9781108525923

Zellman, K.L., Plink-Björklund, P., Fricke, H.C., 2021. Testing hypotheses on signatures of precipitation variability in the river and floodplain deposits of the Paleogene San Juan Basin, New Mexico, U.S.A. Journal of Sedimentary Research. 90, 1770-1801. DOI: 10.2110/jsr.2020.75

FIGURE CAPTIONS

Fig. 1: (A) Study area location; (B) regional stratigraphy, adapted from Bouly and Demassieux (1996), Guillocheau et al. (2000), Herivaux and Marechal (2019) and Duringer et al. (2019). URG = Upper Rhine Graben; and (C) studied outcrops (Vosges mountains), and core (inside the URG), locations.

Fig. 2: Facies associations, their thickness proportion measured for the Lower Grès Vosgien Formation, their respective facies and facies proportions, and a schematic log showing the architectural elements. See further details on architectural elements in section 4.1. and 4.2.

Fig. 3: Facies of the fluvial channel facies association: (A) trough cross-bedded sandstone, St. Red arrow: cross-set of gravelly sandstone. Green arrow: cross-set of slightly gravelly sandstone. Outcrop: LGV7; (B) sigmoidal cross-bedded sandstone, Ss. Gravel content is absent in the topset and concentrated in higher angle foresets. Outcrop: LGV7; (C) laminated mudstone, Fl, between foresets of facies St. Outcrop: LGV1; (D) breccia of angular mud clasts; (E) low-angle cross-bedded sandstone, Sl. Outcrop: LGV5; (F) planar view of parting lineation in facies Sl. Outcrop: LGV7; (G) convex-up top, with internal low-angle truncated cross-bedded sandstone, Sad, interpreted as antidune. Red arrows indicate planes where palaeocurrents, of opposite directions, were measured. Outcrop: LGV9; (H) Facies St, Ss and Sl recognised in core samples. Core EPS1, diameter: 8 cm.

Fig. 4: Downstream transition between LS and TSE, within the same bed, separated by reactivation surfaces. Outcrop: LGV7.
Fig. 5: Fluvial channel facies association (FC) quantitative data. GS = gravelly sandstone; SG = slightly gravelly sandstone; AWG = sandstone apparently without gravel; WG = sandstone without gravel.
Fig. 6: Fluvial architectural elements, their respective quantitative data, and illustration**.** Fig. 7: Aggradational element. (A) Outcrop LGV7; (B) Outcrop LGV10.

Fig. 8: (A) Downstream accretion element (DA). Outcrop: LGV8. (B) Trough simple element (TSE) and aggradational element (AE). Outcrop: LGV4.
Fig. 9: (A) Sigmoidal simple element (SSE), and laminated sand sheet (LS). Outcrop: LGV12. (B) SSE, with the absence of gravel in the topset, concentrated in the foresets. Result of the overpassing process (Allen, 1983b). Outcrop: LGV8.

Fig. 10: Wind- and water-laid facies association (WWL). (A) Translatent wind ripples, Sla. Outcrop: LGV5; (B) (C) centimetre-scale upward transition between facies Sla, Sa (and/or Mb) and Sw, indicating gradual outpace of water-table rise against sediment supply. Outcrop: LGV8 and LGV6, respectively; (D) largest aeolian dune described in the Lower Grès Vosgien Formation, delimited by the dashed yellow line. Outcrop: LGV6; (E) aeolian dune (AD) between hybrid sand sheet (HSS), overlying a blowout hollow surface. Outcrop LGV2; (F) WWL in outcrop (LGV5) and in the EPS1 core samples.

Fig. 11: Wind- and water-laid facies association (WWL) quantitative data.

Fig. 12: (A) Processes involved in generating the wind- and water-laid facies association (WWL); (B) different vertical architectures of the WWL, and their respective proportions of occurrences, recorded in the Lower Grès Vosgien Formation; (C) e.g. Architecture 1. Outcrop: LGV7; (D) e.g. Architecture 3. Outcrop: LGV1; (E) e.g. Architecture 4. Outcrop: LGV5; (F) e.g. Architectures 4 and 5. Outcrop: LGV10; (G) e.g. Architecture 1. Outcrop: LGV5; (H) e.g. Architecture 2. Outcrop: LGV7; (I) distribution of thickness of each architecture presented on (B).
Fig. 13: Vertical and lateral architecture distribution of the Lower Grès Vosgien Formation, in an outcrop scale. Outcrop: LGV7.

Fig. 14: Block diagram of wind- and water-laid facies association (WWL), representing two distinct temporal moments. (A) Formation of hybrid sand sheet architectural element, influenced by water-table level close to the depositional surface, and by ephemeral floods; (B) WWL during low water-table level. Sand deflation by winnowing, leaving behind deflation lag and blowout hollows, followed by accumulation and migration of aeolian dunes.

Fig. 15: (A) Log from the core EPS1 exhibiting the intercalations between fluvial channel facies association (FC), and wind- and water-laid facies association (WWL) recorded within the upper 100 m of the Lower Grès Vosgien Formation (LGV); (B) fluvial cross-set thickness occurrences along 100 m of the EPS1 core, which represents the top of the LGV (Aichholzer, 2019). Rs and p-value in blue, all cross-sets (red and blue dots) are analysed. In red, only cross-sets thicker than 50 cm are analysed. Thinning-upward trends are observed, however, a strong correlation between cross-set thickness and depth is only observed for the larger (>50 cm) cross-sets; (C) strong correlation between FC thickness and depth; (D) weak negative correlation between WWL thickness and depth. However, the high *p*-value indicates that the dataset used for this analysis is not enough.

TABLE CAPTIONS

Table 1: Classes of gravel content in sandstone, and field criteria for their definition.

Class	Code	Class criteria
Sandstone without gravel	WG	No gravel clasts present within the set
Sandstone apparently without gravel	AWG	Difficult to find gravel clasts. Sometimes, a single granule or pebble within the set (i.e., ≪1 %)
Slightly gravelly sandstone	SG	Easy to find granules and pebbles within the set (up to 5 %, Folk et al., 1970)
Gravelly sandstone	GS	Rich in granules, pebbles, and occasionally cobbles (5 %–30 %, Folk et al., 1970)

Table 2: Sedimentary facies observed in the Lower Grès Vosgien Formation.

Code	Facies description	Facies interpretation
St	Fine- to very coarse-grained sandstone, with trough cross-stratification; poorly- to well-sorted; it may have abundant quartz and quartzite clasts, occasionally up to cobble size, and 1–5 cm mud clasts, occasionally up to 35 cm; normal gradation in foreset laminae. Set thickness varies from 10 cm up to 1.8 m. Presence of reactivation surfaces. Example: Fig. 3A.	Migration of subaqueous sinuous-crested and linguoid (3-D) dunes (Miall, 2006). Lower flow-regime (Zellman et al., 2021).
Sl	Fine- to very coarse-grained sandstone, with flat to low-angle cross-stratification (Fig. 3E), and, locally, convex-up laminations; poorly- to well-sorted; it may present abundant quartz and quartzite clasts up to pebble size; sub-angular to rounded grains. Parting lineation can be present when observed in planar view. Set thickness varies from 10 cm up to 1.75 m. Example: Fig. 3E, F and H.	Washed-out dunes (Miall, 1988, 2006), deposited in transitional flow-regime (Zellman et al., 2021); or deposition by breaking and upstream migrating antidunes, deposited under upper flow-regime (Fielding, 2006; Duller et al., 2008; Lang and Winsemann, 2013).
Ss	Medium- to very coarse-grained sandstone, with sigmoidal cross-stratification; poorly- to well-sorted; it may present abundant quartz and quartzite clasts up to pebble size; sub-angular to rounded grains. Set thickness varies from 25 cm up to 1.4 m. Example: Fig. 3B, and H.	Humpback dunes (Sauderson and Lockett, 1983; Lang et al., 2021) formed at transitional flow-regime (Plink-Björklund, 2015), or by near-bed suspended sediment concentration (Bridge and Best, 1988). Bed features are formed by high-stage currents, transitioning from dune to plane bed (Røe, 1987). Different trajectories of the topset–foreset-transition point to different rates of deposition (Lang and Winsemann, 2013)
Sp	Medium- to coarse-grained sandstone, with planar cross-stratification; moderately- to well-sorted; it may present scattered granules and pebbles. Set thickness varies from 45 cm up to 75 cm.	Migration of subaqueous straight-crested dunes, under lower flow-regime (Miall, 2006).
Sad	Medium-grained sandstone, with internal low-angle, truncated, cross-stratification, dipping in the opposite direction of the dominant cross-stratified sets above and below; records convex-up top; poorly- to well-sorted. Set thickness varies from 7 cm up to 20 cm. Example: Fig. 3G.	Upstream migrating subaqueous antidunes under supercritical flow (Alexander et al., 2001; Fielding, 2006; Cartigny et al., 2014)
Sr	Fine- to medium-grained sandstone, with asymmetric ripple cross-lamination; moderately- to well-sorted; few centimetre set thickness, forming up to 10 cm thick co-sets.	Migration of unidirectional subaqueous ripples. Lower flow-regime (Miall, 1977)
Sta	Fine- to medium-grained sandstone, with trough cross-stratification; moderately- to well-sorted; sub- to well-rounded grains; occasionally toesets consist of millimetrically spaced inverse graded lamination, and pin-stripe lamination. Set thickness varies from 10 cm up to 2.7 m. Occasionally records more than one set superimposed. Example: Fig. 10D and E.	Migration of crescentic aeolian dunes (Kocurek, 1991). Slip-face with intercalation of grain-fall and grain-flow (Kocurek, 1991). Occasionally forming draas (Kocurek, 1991).
Sla	Very fine- to medium-grained sandstone, showing grain size bimodality; flat to low-angle lamination; moderately- to well-sorted; sub- to well-rounded grains; pin-stripe laminations (Fryberger and Schenk, 1988), occasionally preserved inverse graded lamination; and concentration of coarser grains in lenses (~5 cm width, 5 mm thick). Package thickness varies from 3 cm up to 40 cm. Example: Fig. 10A, B and C.	Translatent wind ripple climbing at sub-critical angles (Hunter, 1977; Cain and Mountney, 2009). Occasional occurrence of granule ripples (Fryberger et al., 1992).
Fl	Laminated mudstone, which might present bioturbation. Layer thickness varies from 1 mm to 15 cm. Often represented by levels with large mud cracks; laterally discontinuous due to erosion by succeeding flows. Example: Fig. 3D.	Deposition of suspended load by settling out in standing water (Miall, 2006)
Mb	Mudstone, with millimetric wrinkled lamination; laterally discontinuous; individual laminae thickness up to 1 mm; dominantly interfingered with facies Sla, occasionally at foreset base of facies Sta, sometimes with Sw; package thickness where facies Mb is interfingered (Sla and Sw) varies from 5 cm up to 25 cm. Example: Fig. 10B.	Microbial mat formed rapidly between clastic depositional events, on wet substratum, resulting in microbially induced sedimentary structure (MISS) (Gerdes, 2007; Basilici et al., 2020)
Sw	Very fine- to medium-grained sandstone, with symmetric ripple-lamination; well-sorted; occasionally capped by mudstone laminae. Example: Fig. 10B and C	Sedimentation within oscillating ponds or shallow lakes, during windy periods (Ribes et al., 2015), followed by calm sedimentation (Miall, 2006)
Sa	Fine-grained sandstone, with wrinkled lamination; poorly- to well-sorted; individual lamina thickness up to 1 cm. Set thickness up to 20 cm, interfingered with facies Sla and Slw. Example: Fig. 10C.	Adhesion of grains transported by the wind to a damp surface (Kocurek and Fielder, 1982).
Sm	Fine-grained sandstone, with no recognisable structures; well-sorted. Set thickness varies from 5 cm up to 15 cm.	Rapid deposition of hyperconcentrated subaqueous gravity flow (Miall, 2006; Scherer et al., 2015), or appear massive due to diagenetic effects (Miall, 2006).

Table 3: Fluvial channel facies association (FC) dataset concerning architectural elements proportions; mean set thickness of sets below 78 cm, within the aggradational element (AE) (M.S.T.< 78 cm); coefficient of variance of cross-set thickness in the AE (CV) (calculated where data of minimum 30 sets were available); mean original dune height (H_m), (Equation 1); and mean flow depth (*d)* (Equation 2). The dataset is presented by individual FC, bounded by WWL deposits. The term "complete FC unit" refers to FC deposits where upper and lower boundaries are recognized. Where more than one FC unit is identified in the same outcrop, the point (outcrop code) is followed by a sequence number (e.g., LGV2-2). "Incomplete" refers to outcrops where lower or upper FC boundaries were not exposed. DA = downstream accretion element; TSE = trough simple element; SSE = sigmoidal simple element; LS = laminated sand sheet. Grey areas refer to no data available.

Point	Complete FC unit thickness (m)	Architectural elements proportion (%)					M.S.T. (cm) <78 cm	C.V. (AE)	*Hm* (m)		*d* (m)	
		AE	DA	TSE	SSE	LS			Min (x2.2)	Max (x3.6)	Min (x6)	Max (x10)
LGV1	4.0											
LGV2-1	5.4											
LGV2-2	3.7											
LGV3	31.5	68		14	18		29	0.51	0.70	1.15	4.2	11.5
LGV4-1	10.3	33	27	20		20	21	-	0.51	0.83	3.0	8.3
LGV4-2	5.7	46	40		14		29	-	0.70	1.15	4.2	11.5
LGV5-1	4.8											
LGV5-2	9.1											
LGV6	Incomplete	100					24	-	0.57	0.93	3.4	9.3
LGV7	12.8	53	12	9	8	18	24	0.48	0.58	0.95	3.5	9.5
LGV8-1	3.6	27			44	29	36	-	0.87	1.43	5.2	14.3
LGV8-2	6.1	100					21	-	0.51	0.83	3.0	8.3
LGV9	Incomplete	66	8	20		5	22	0.50	0.53	0.87	3.2	8.7
LGV10	1.5	100					18	-	0.44	0.71	2.6	7.1
LGV11	8.1											
LGV12	Incomplete	29		32	22	17	10	-	0.24	0.40	1.5	4.0

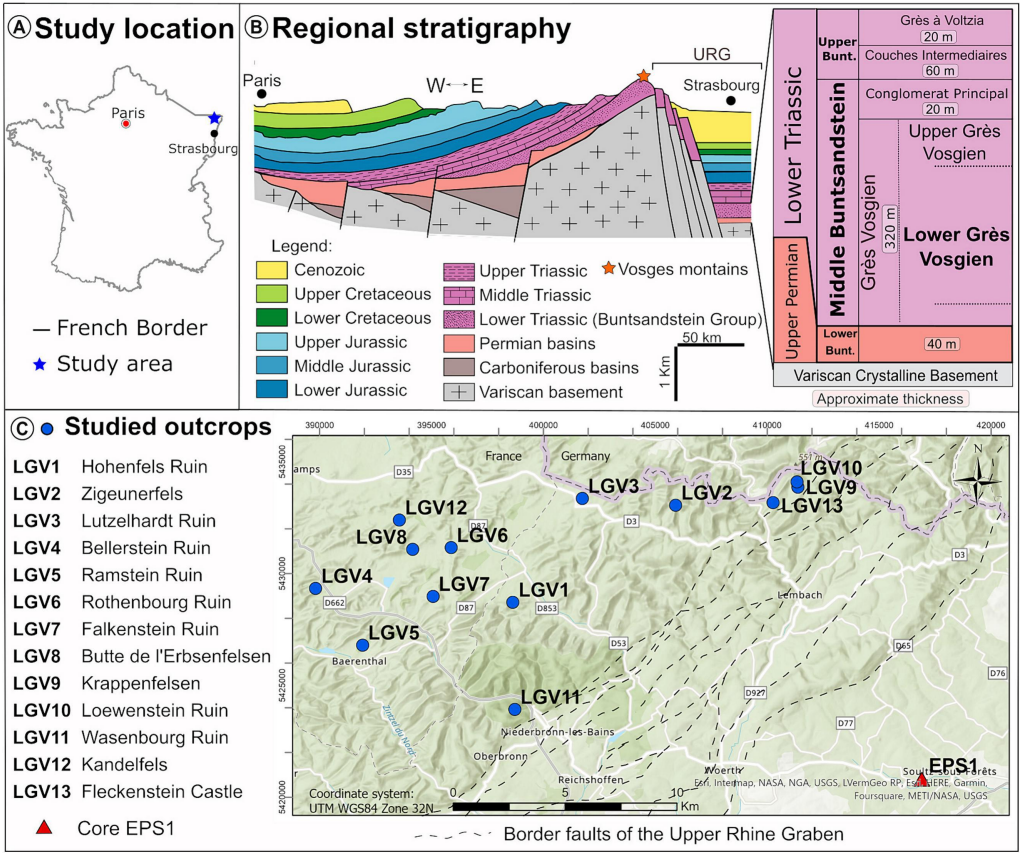
Ⓐ Study location
Paris
Strasbourg
— French Border
★ Study area
Ⓑ Regional stratigraphy
Paris
W → E
URG
Strasbourg
Legend:
Cenozoic
Upper Cretaceous
Lower Cretaceous
Upper Jurassic
Middle Jurassic
Lower Jurassic
Upper Triassic
Middle Triassic
Lower Triassic (Buntsandstein Group)
Permian basins
Carboniferous basins
Variscan basement
Vosges montains
50 km
1 Km
Lower Triassic
Upper Permian
Upper Bunt.
Middle Buntsandstein
Lower Bunt.
Grès à Voltzia
20 m
Couches Intermediaires
60 m
Conglomerat Principal
20 m
Grès Vosgien
320 m
Upper Grès Vosgien
Lower Grès Vosgien
40 m
Variscan Crystalline Basement
Approximate thickness
Ⓒ Studied outcrops
LGV1 Hohenfels Ruin
LGV2 Zigeunerfels
LGV3 Lutzelhardt Ruin
LGV4 Bellerstein Ruin
LGV5 Ramstein Ruin
LGV6 Rothenbourg Ruin
LGV7 Falkenstein Ruin
LGV8 Butte de l'Erbsenfelsen
LGV9 Krappenfelsen
LGV10 Loewenstein Ruin
LGV11 Wasenbourg Ruin
LGV12 Kandelfels
LGV13 Fleckenstein Castle
Core EPS1
390000
395000
400000
405000
410000
415000
420000
5435000
5430000
5425000
5420000
France
Germany
LGV1
LGV2
LGV3
LGV4
LGV5
LGV6
LGV7
LGV8
LGV9
LGV10
LGV11
LGV12
LGV13
EPS1
Baerenthal
Lembach
Niederbronn-les-Bains
Oberbronn
Reichshoffen
Woerth
Zinsel du Nord
D35
D87
D3
D662
D853
D53
D65
D76
D927
D77
Coordinate system:
UTM WGS84 Zone 32N
0
5
10
Km
Esri, Intermap, NASA, NGA, USGS, LVermGeo RP, Esri, HERE, Garmin, Foursquare, METI/NASA, USGS
Border faults of the Upper Rhine Graben

Figure 1

Facies association	Facies	Schematic log	
		Facies	Architectural element
Fluvial channel (FC) 93%	*Thickness* St = 72.9% Sl = 12.9% Ss = 12.4% Sp = 1.1% Sad = 0.3% Sr = 0.3% Fl = 0.1%	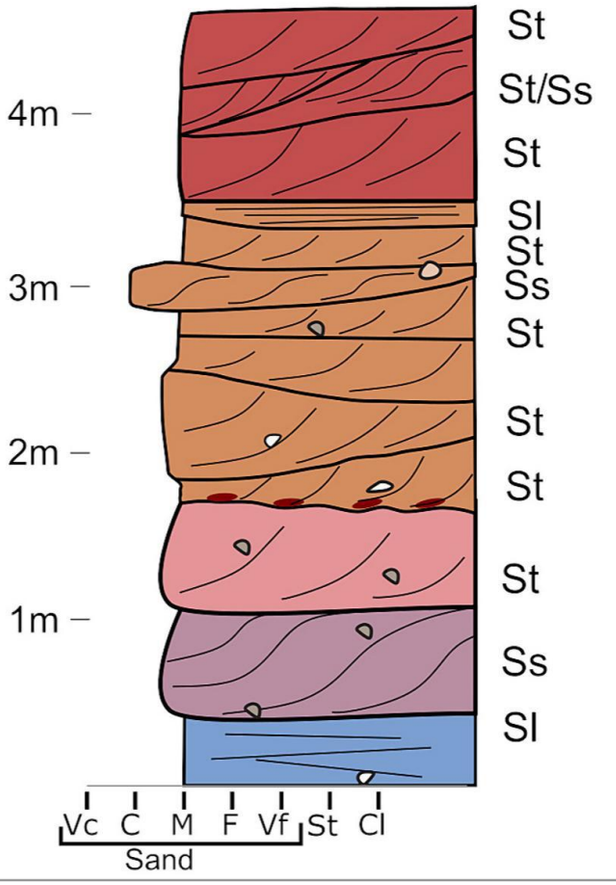	Downstream accretion element (DA) Aggradational element (AE) Trough simple element (TSE) Sigmoidal simple element (SSE) Laminated sand sheet element (LS)
Wind- and water-laid (WWL) 7%	*Thickness* Sla + Sa + Mb + Sw = 40% Sta = 60% *Occurrence* Sla + Sa + Mb + Sw = 57% Sta = 43%	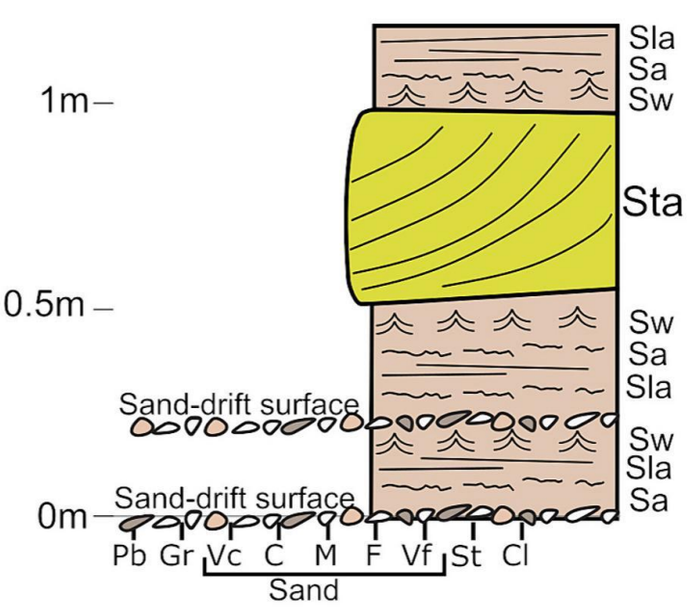	Hybrid sand sheet (HSS) Aeolian dune (AD) Hybrid sand sheet (HSS)

Figure 2

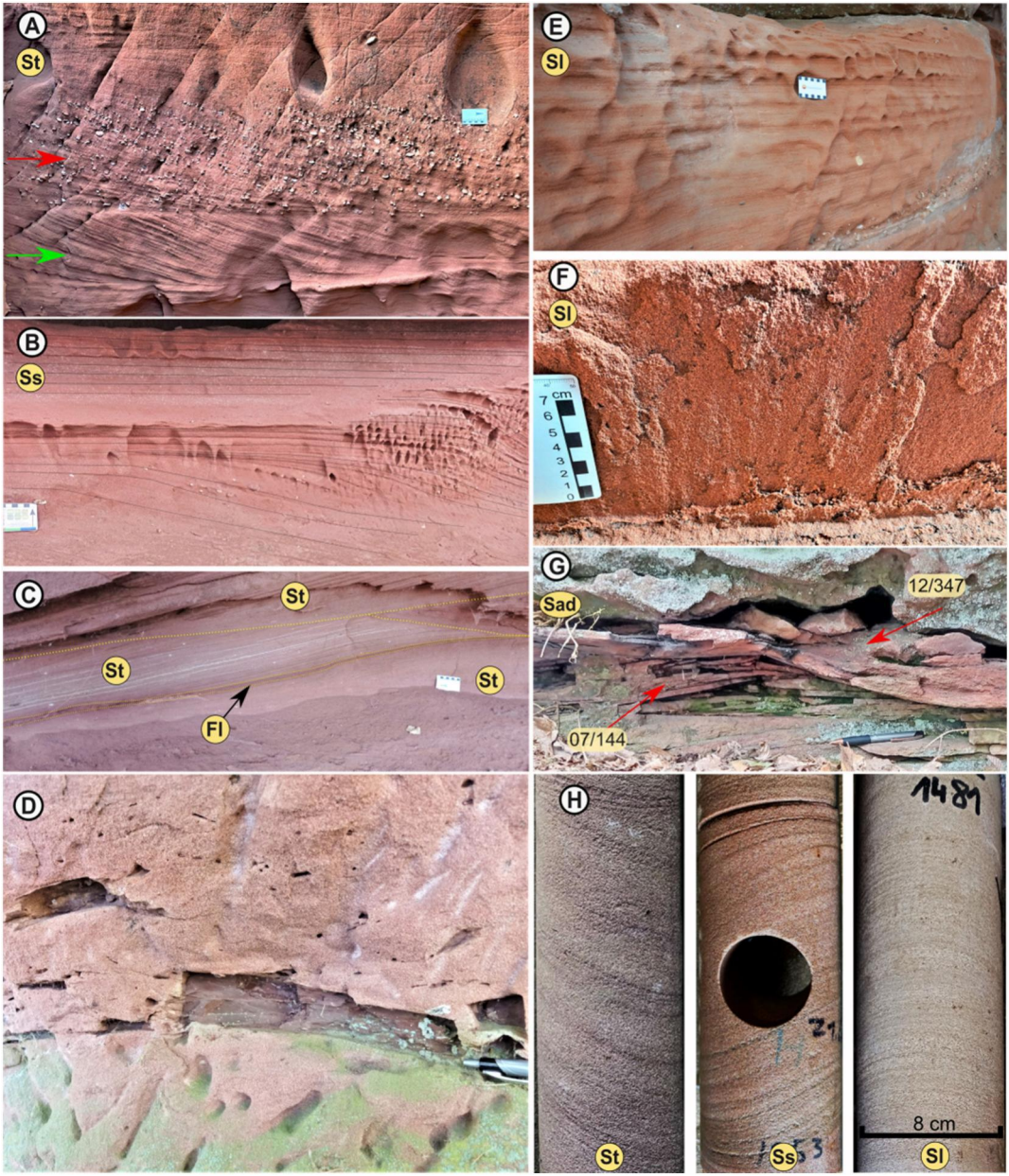
A
St
B
Ss
C
St
St
St
Fl
D
E
Sl
F
Sl
7 cm
6
5
4
3
2
1
0
G
Sad
12/347
07/144
H
St
Ss
Sl
8 cm

Figure 3

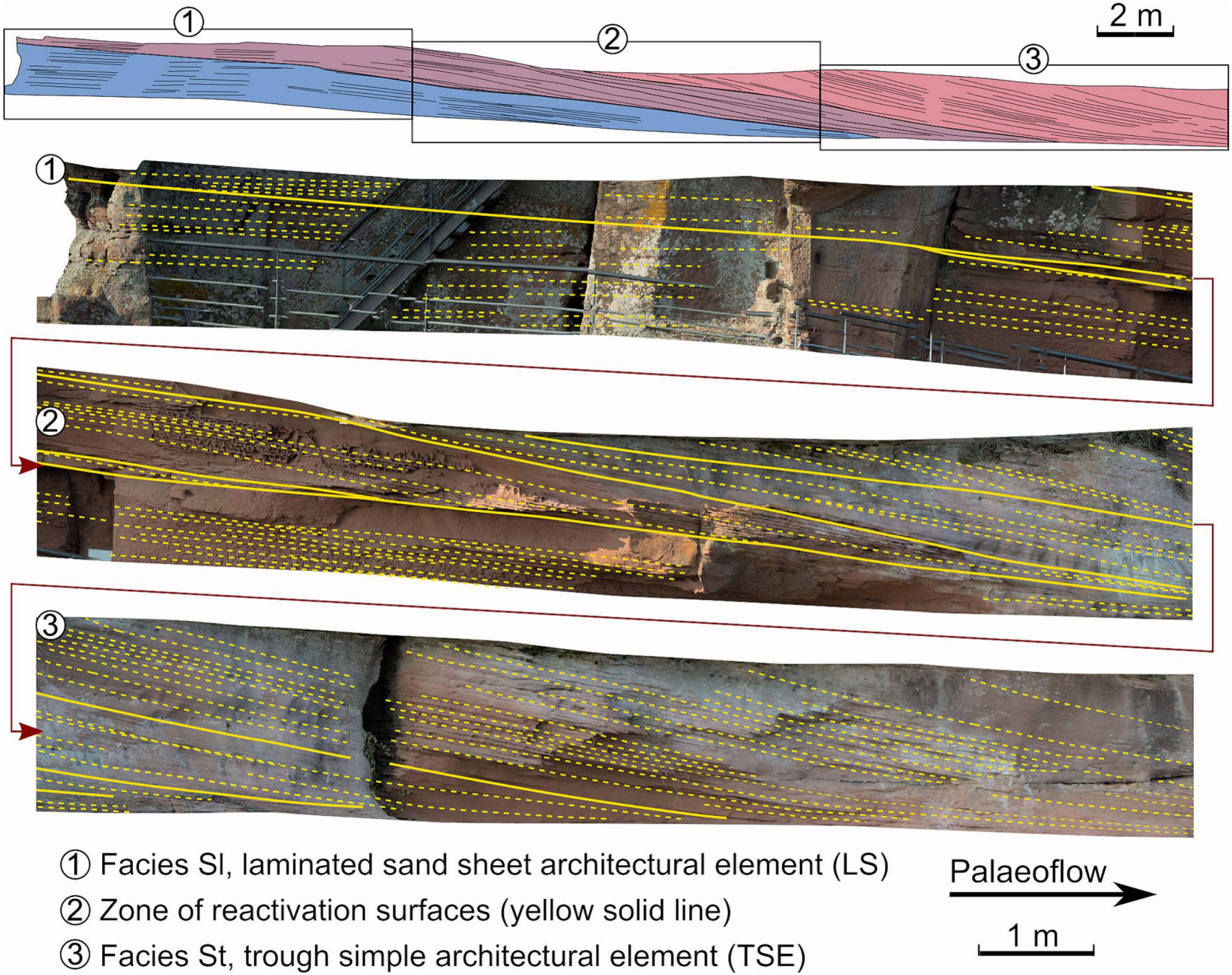
①
②
③
2 m
① Facies Sl, laminated sand sheet architectural element (LS)
② Zone of reactivation surfaces (yellow solid line)
③ Facies St, trough simple architectural element (TSE)
Palaeoflow
1 m

Figure 4

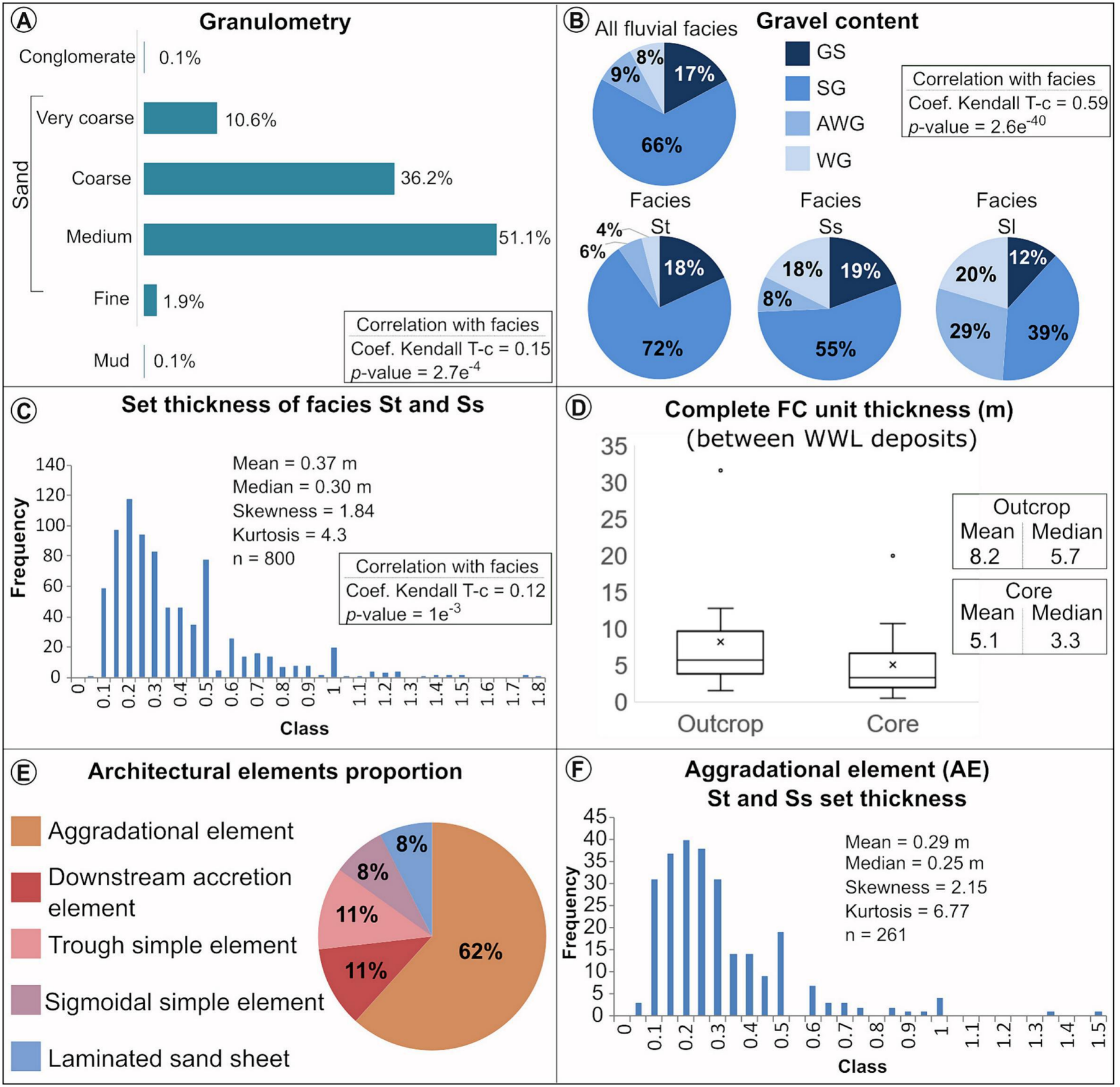
A
Granulometry
Conglomerate
0.1%
Sand
Very coarse
10.6%
Coarse
36.2%
Medium
51.1%
Fine
1.9%
Mud
0.1%
Correlation with facies
Coef. Kendall T-c = 0.15
p-value = 2.7e-4
B
All fluvial facies
Gravel content
GS
SG
AWG
WG
8%
17%
9%
66%
Correlation with facies
Coef. Kendall T-c = 0.59
p-value = 2.6e-40
Facies St
4%
6%
18%
72%
Facies Ss
18%
19%
8%
55%
Facies Sl
20%
12%
29%
39%
C
Set thickness of facies St and Ss
Mean = 0.37 m
Median = 0.30 m
Skewness = 1.84
Kurtosis = 4.3
n = 800
Correlation with facies
Coef. Kendall T-c = 0.12
p-value = 1e-3
Frequency
Class
D
Complete FC unit thickness (m)
(between WWL deposits)
Outcrop
Mean 8.2
Median 5.7
Core
Mean 5.1
Median 3.3
Outcrop
Core
E
Architectural elements proportion
Aggradational element
Downstream accretion element
Trough simple element
Sigmoidal simple element
Laminated sand sheet
62%
11%
11%
8%
8%
F
Aggradational element (AE)
St and Ss set thickness
Mean = 0.29 m
Median = 0.25 m
Skewness = 2.15
Kurtosis = 6.77
n = 261
Frequency
Class

Figure 5

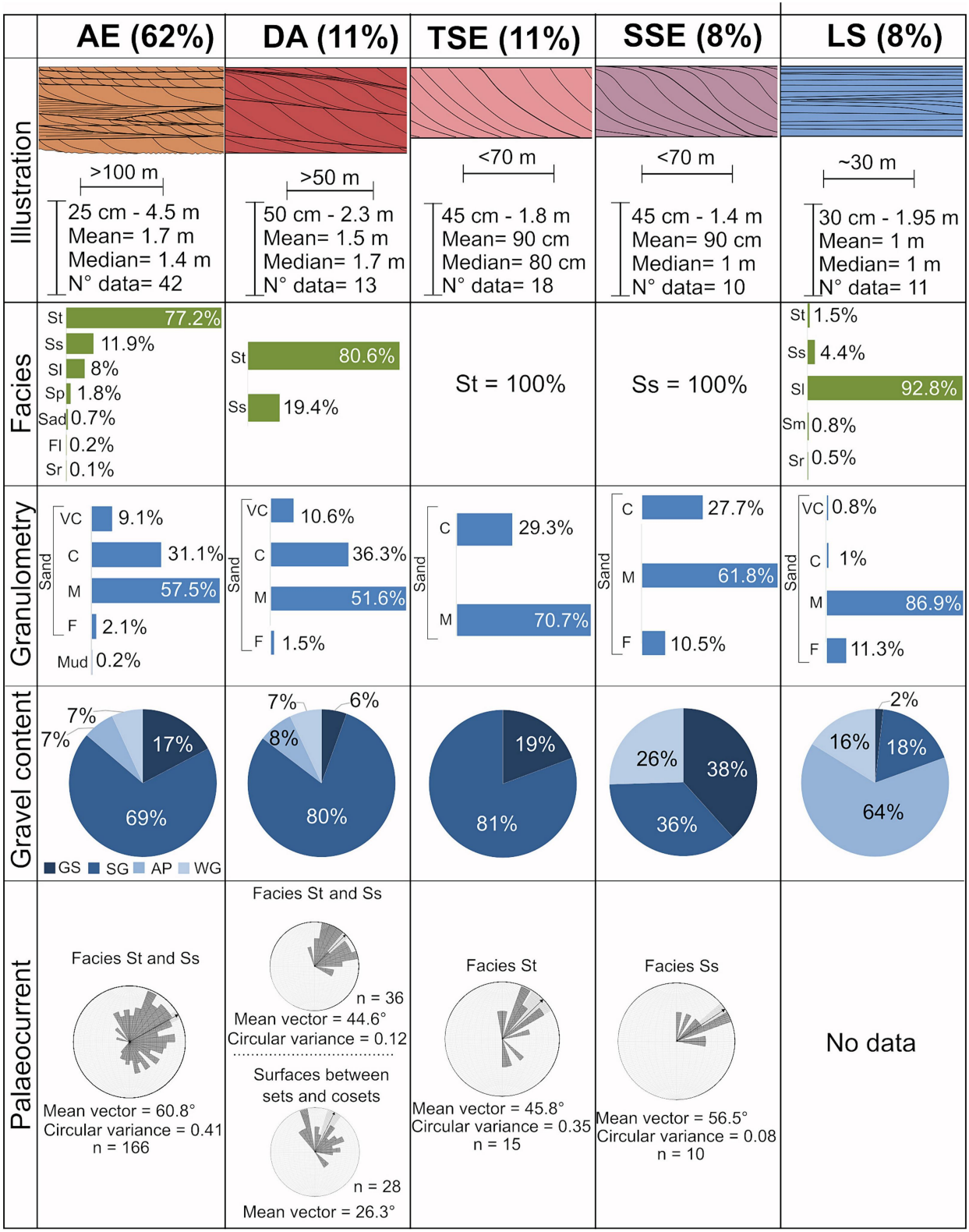
AE (62%)
DA (11%)
TSE (11%)
SSE (8%)
LS (8%)
Illustration
>100 m
25 cm - 4.5 m
Mean= 1.7 m
Median= 1.4 m
N° data= 42
>50 m
50 cm - 2.3 m
Mean= 1.5 m
Median= 1.7 m
N° data= 13
<70 m
45 cm - 1.8 m
Mean= 90 cm
Median= 80 cm
N° data= 18
<70 m
45 cm - 1.4 m
Mean= 90 cm
Median= 1 m
N° data= 10
~30 m
30 cm - 1.95 m
Mean= 1 m
Median= 1 m
N° data= 11
Facies
St 77.2%
Ss 11.9%
Sl 8%
Sp 1.8%
Sad 0.7%
Fl 0.2%
Sr 0.1%
St 80.6%
Ss 19.4%
St = 100%
Ss = 100%
St 1.5%
Ss 4.4%
Sl 92.8%
Sm 0.8%
Sr 0.5%
Granulometry
Sand
VC 9.1%
C 31.1%
M 57.5%
F 2.1%
Mud 0.2%
VC 10.6%
C 36.3%
M 51.6%
F 1.5%
C 29.3%
M 70.7%
C 27.7%
M 61.8%
F 10.5%
VC 0.8%
C 1%
M 86.9%
F 11.3%
Gravel content
7%
7%
17%
69%
GS SG AP WG
7%
6%
8%
80%
19%
81%
26%
38%
36%
2%
16%
18%
64%
Palaeocurrent
Facies St and Ss
Mean vector = 60.8°
Circular variance = 0.41
n = 166
Facies St and Ss
n = 36
Mean vector = 44.6°
Circular variance = 0.12
Surfaces between sets and cosets
n = 28
Mean vector = 26.3°
Facies St
Mean vector = 45.8°
Circular variance = 0.35
n = 15
Facies Ss
Mean vector = 56.5°
Circular variance = 0.08
n = 10
No data

Figure 6

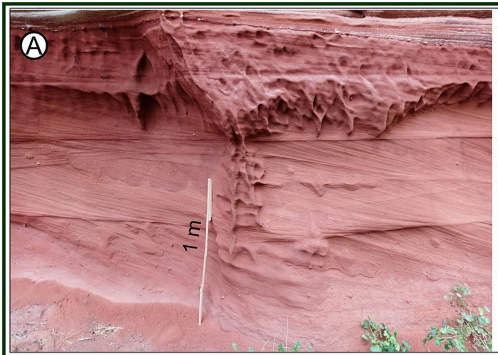

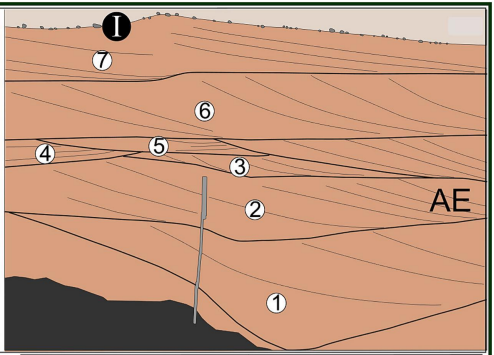

I Architectual element upper boundary coincident with the fluvial channel facies association (FC) upper boundary. Marked by an aeolian deflation lag. Contact with WWL deposits.

* dd = dip direction; da = dip angle

Set	Facies	Foreset dd°	Basal surface da°/dd°
1	St	090°	11°/085°
2	St	073°	02°/052°
3	St	076°	03°/110°
4	St	140°	04°/290°
5	St	114°	03°/325°
6	St	108°	Horizontal
7	Ss	102°	Horizontal

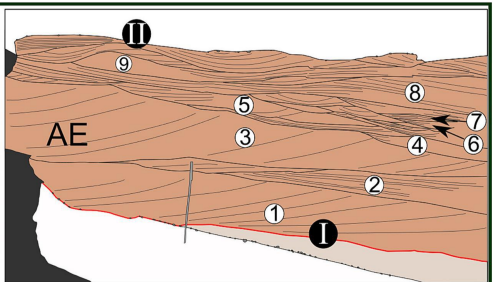

I Architectual element lower boundary, coincident with FC lower boundary, in contact with WWL deposits

II Architectual element upper boundary, coincident with FC upper boundary, marked by an aeolian deflation lag.

Example of a complete FC deposit (between WWL)

Set	Facies	Foreset dd°	Basal surface da°/dd°
1	St	120°	**I** Erosive
2	Sl	—	03°/263°
3	St	180°	08°/239°
4	St	106°	05°/284°
5	St	014°	14°/057°
6	St	357°	No data
7	Ss	013°	08°/336°
8	Ss	151°	09°/315°
9	Sl	—	06°/345°

Figure 7

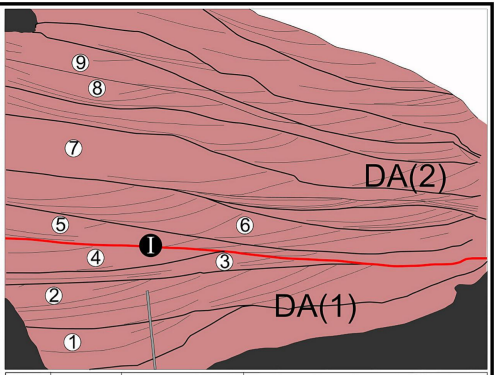

Set	Facies	Foreset dd°	Basal surface da°/dd°
1	St	026°	13°/035°
2	St	019°	10°/340°
3	St	028°	14°/328°
4	St	034°	17°/336°
5	St	343°	I 04°/132°
6	St	018°	13°/321°

Set	Facies	Foreset dd°	Basal surface da°/dd°
7	St	036°	12°/340°
8	St	071°	No data
9	St	067°	07°/060°

I Bounding surface between elemens DA(1) and DA(2)

* dd = dip direction; da = dip angle

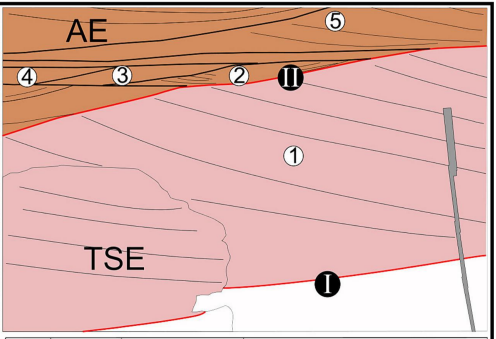

I Architectural element lower boundary

II Erosional surface between elemens TSE and AE.

Set	Facies	Foreset dd°	Basal surface da°/dd°
1	St	016°	I 02°/030°
2	St	104°	II 05°/250°
3	St	125°	No data
4	St	129°	No data
5	St	003°	Horizontal

Figure 8

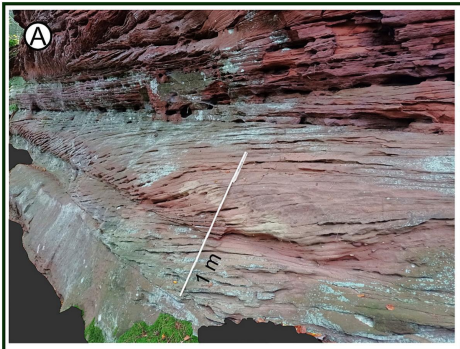

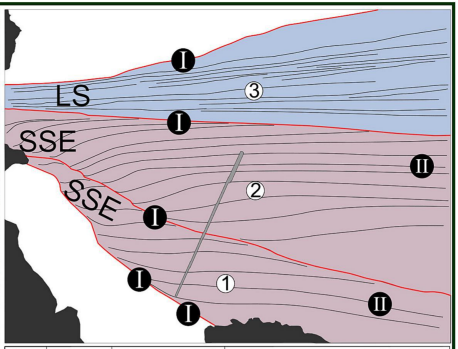

I Horizontal to sub-shorizontal upper, and lower bounding surfaces of architectural elements SSE and LS

II Low-angle dipping topset of facies Ss

Set	Facies	Foreset dd°	Basal surface da°/dd°
1	Ss	028°	Horizontal
2	Ss	020°	03/075°
3	Sl	—	Horizontal

* dd = dip direction; da = dip angle

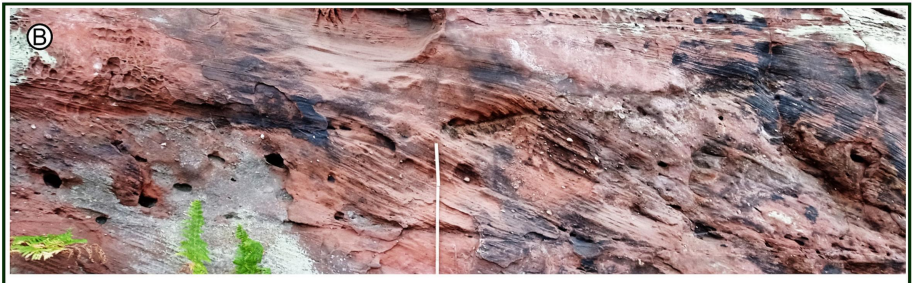

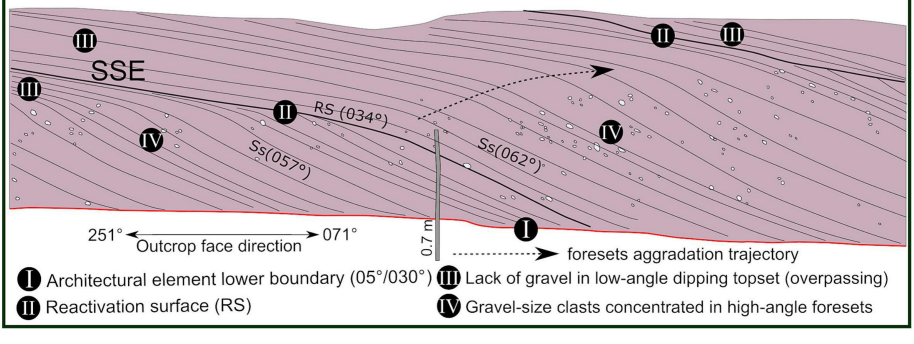

I Architectural element lower boundary (05°/030°)

II Reactivation surface (RS)

III Lack of gravel in low-angle dipping topset (overpassing)

IV Gravel-size clasts concentrated in high-angle foresets

Figure 9

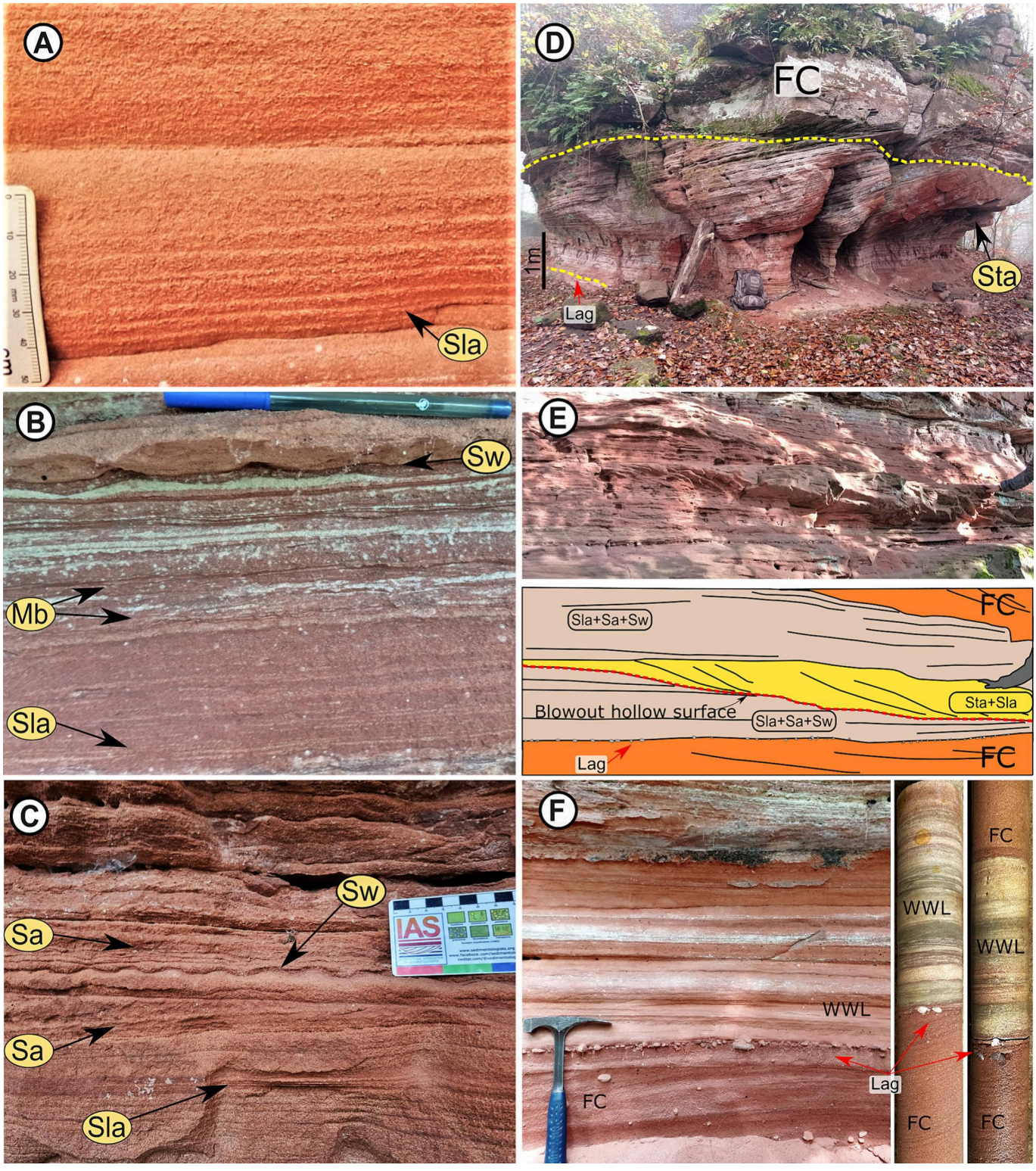
A
Sla
D
FC
1m
Lag
Sta
B
Sw
Mb
Sla
E
Sla+Sa+Sw
FC
Blowout hollow surface
Sta+Sla
Sla+Sa+Sw
Lag
FC
C
Sw
Sa
Sa
Sla
IAS
F
WWL
FC
Lag
WWL
FC
WWL
FC

Figure 10

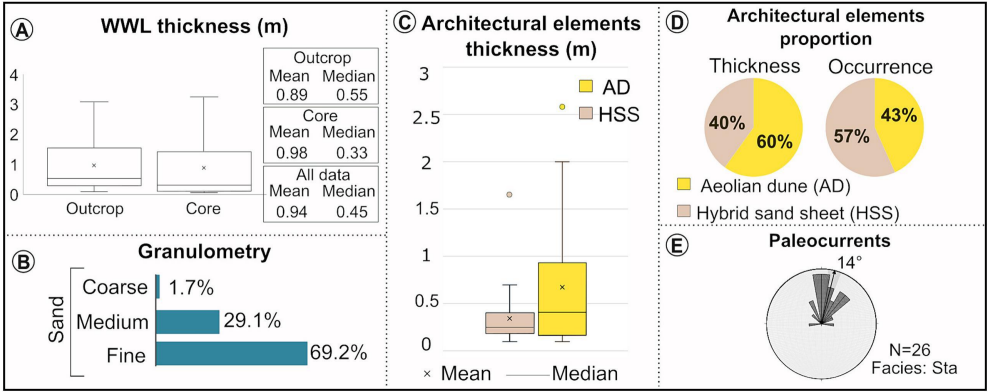
A
WWL thickness (m)
Outcrop
Mean Median
0.89 0.55
Core
Mean Median
0.98 0.33
All data
Mean Median
0.94 0.45
4
3
2
1
0
Outcrop
Core
B
Granulometry
Sand
Coarse 1.7%
Medium 29.1%
Fine 69.2%
C Architectural elements thickness (m)
AD
HSS
3
2.5
2
1.5
1
0.5
0
× Mean
Median
D
Architectural elements proportion
Thickness
Occurrence
40%
60%
57%
43%
Aeolian dune (AD)
Hybrid sand sheet (HSS)
E
Paleocurrents
14°
N=26
Facies: Sta

Figure 11

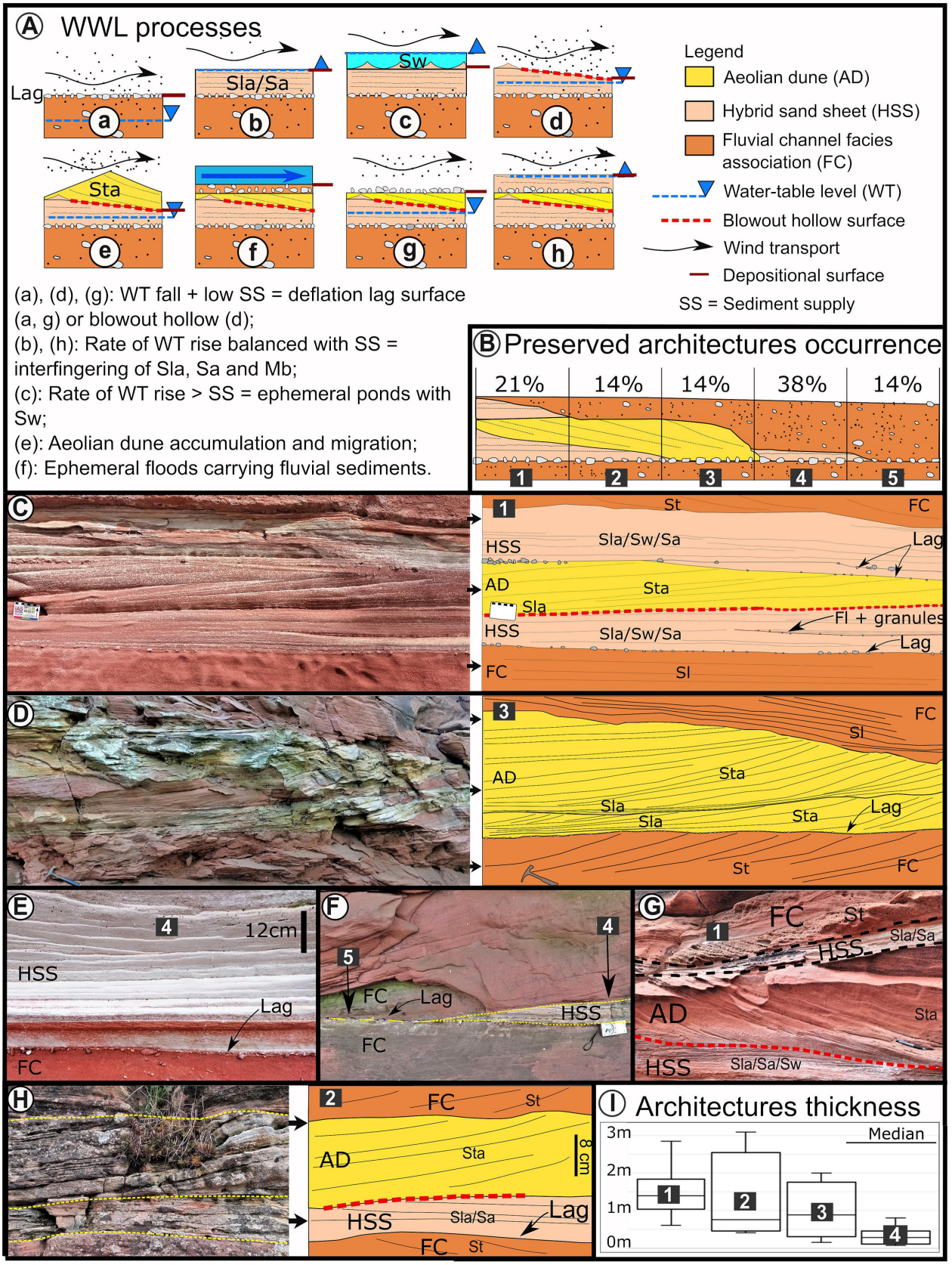
Ⓐ WWL processes
Lag
Sla/Sa
Sw
Sta
a
b
c
d
e
f
g
h
Legend
Aeolian dune (AD)
Hybrid sand sheet (HSS)
Fluvial channel facies association (FC)
Water-table level (WT)
Blowout hollow surface
Wind transport
Depositional surface
SS = Sediment supply
(a), (d), (g): WT fall + low SS = deflation lag surface (a, g) or blowout hollow (d);
(b), (h): Rate of WT rise balanced with SS = interfingering of Sla, Sa and Mb;
(c): Rate of WT rise > SS = ephemeral ponds with Sw;
(e): Aeolian dune accumulation and migration;
(f): Ephemeral floods carrying fluvial sediments.
Ⓑ Preserved architectures occurrence
21%
14%
14%
38%
14%
1
2
3
4
5
Ⓒ
St
FC
HSS
Sla/Sw/Sa
Lag
AD
Sta
Sla
Fl + granules
Sl
Ⓓ
Ⓔ
12cm
Ⓕ
Ⓖ
Sla/Sa
Sla/Sa/Sw
Ⓗ
∞ cm
Ⓘ Architectures thickness
Median
3m
2m
1m
0m

Figure 12

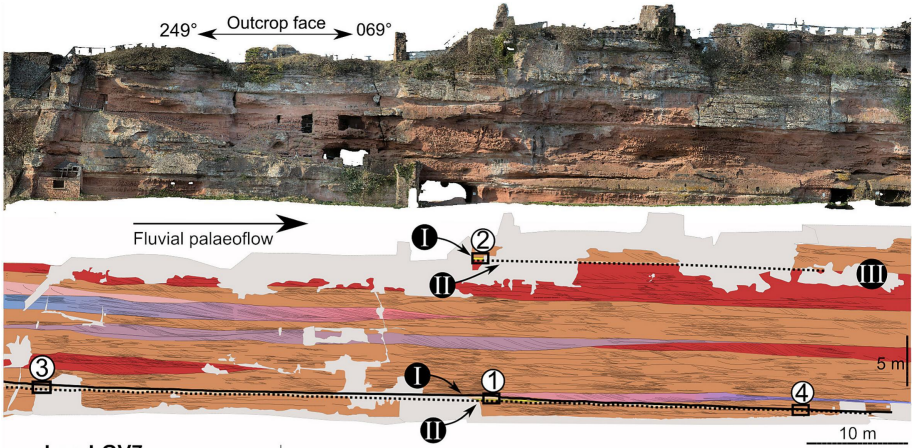

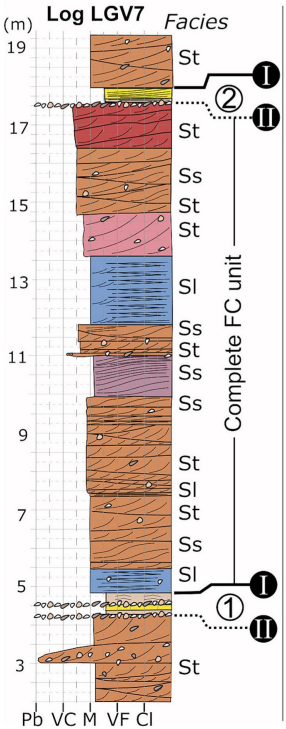

Fluvial channel facies association (FC) architecture

Architectural elements

- Aggradational element (AE)
- Downstream accretion element (DA)
- Trough simple element (TSE)
- Sigmoidal simple element (SSE)
- Laminated sand sheet (LS)

I FC lower boundary

Wind- and water-laid facies association (WWL) architecture

Architectural elements

- Hybrid sand sheet (HSS)
- Aeolian dune (AD)

II WWL lower boundary (sand-drift surface)

III Lateral erosion of WWL and sand-drift surface

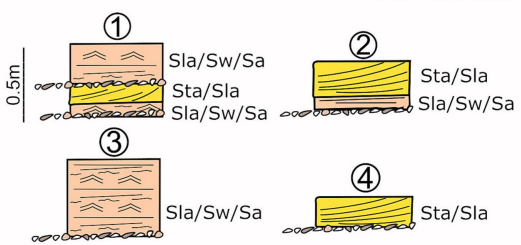

Figure 13

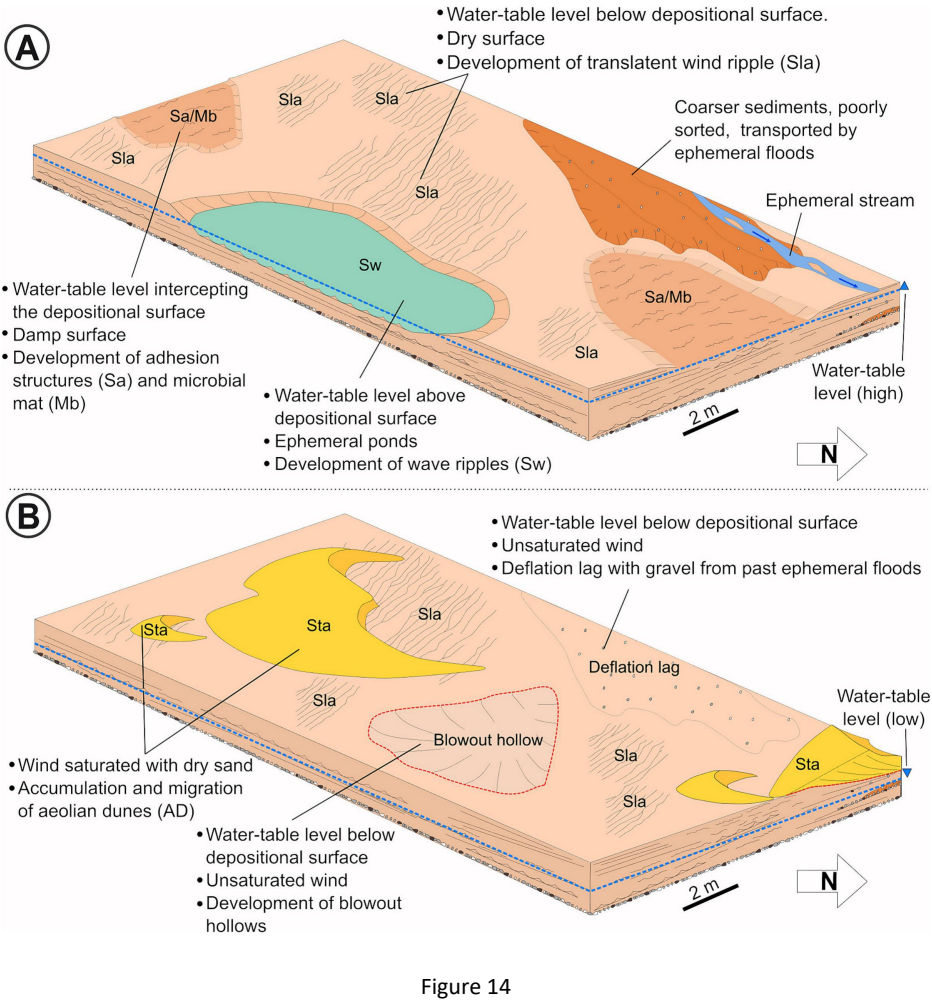
A
• Water-table level below depositional surface.
• Dry surface
• Development of translatent wind ripple (Sla)
Sa/Mb
Sla
Sla
Sla
Sla
Coarser sediments, poorly sorted, transported by ephemeral floods
Ephemeral stream
Sw
Sa/Mb
Sla
Water-table level (high)
• Water-table level intercepting the depositional surface
• Damp surface
• Development of adhesion structures (Sa) and microbial mat (Mb)
• Water-table level above depositional surface
• Ephemeral ponds
• Development of wave ripples (Sw)
2 m
N
B
• Water-table level below depositional surface
• Unsaturated wind
• Deflation lag with gravel from past ephemeral floods
Sta
Sta
Sla
Deflation lag
Sla
Water-table level (low)
Blowout hollow
Sla
Sta
Sla
• Wind saturated with dry sand
• Accumulation and migration of aeolian dunes (AD)
• Water-table level below depositional surface
• Unsaturated wind
• Development of blowout hollows
2 m
N

Figure 14

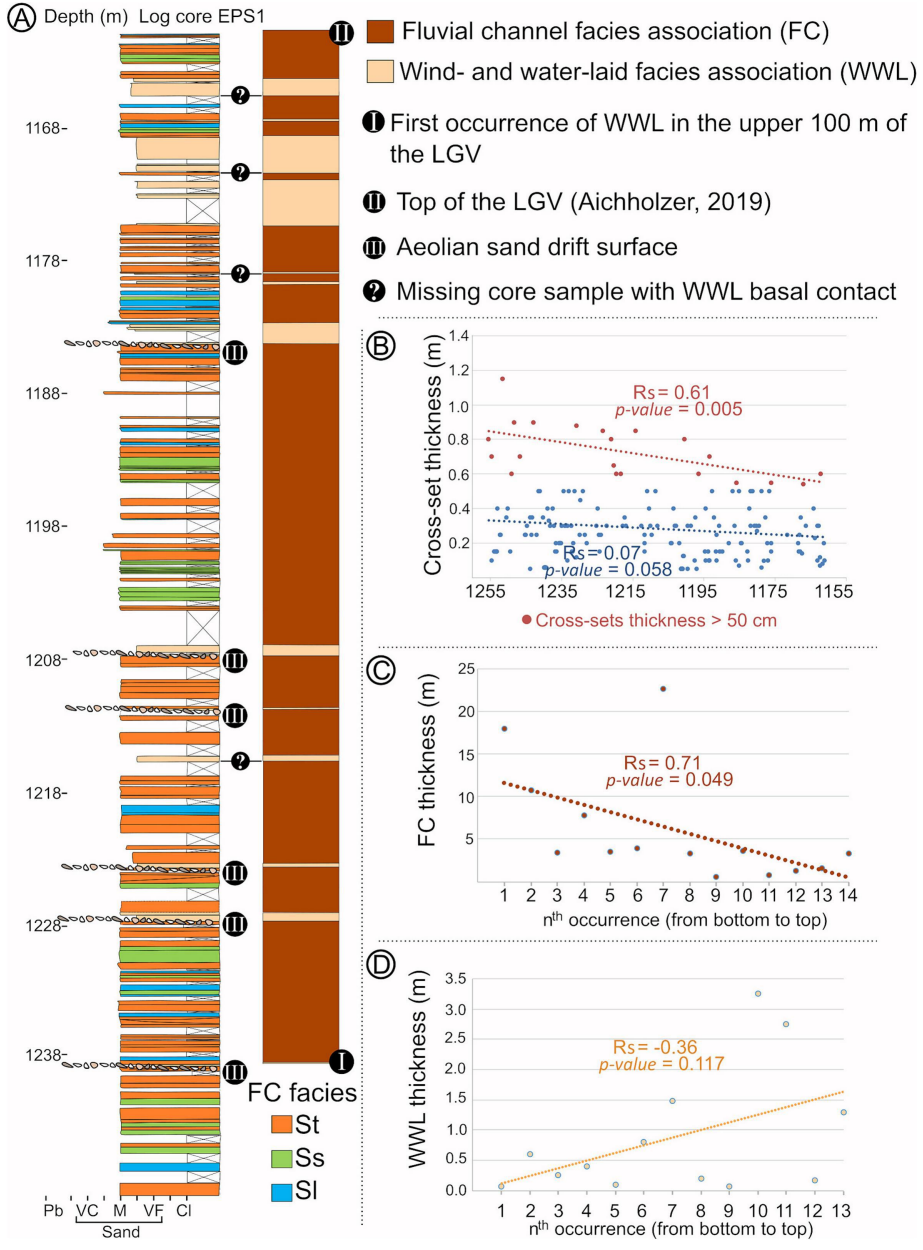
Ⓐ Depth (m) Log core EPS1
1168
1178
1188
1198
1208
1218
1228
1238
Pb VC M VF Cl
Sand
FC facies
St
Ss
Sl
Fluvial channel facies association (FC)
Wind- and water-laid facies association (WWL)
❶ First occurrence of WWL in the upper 100 m of the LGV
❷ Top of the LGV (Aichholzer, 2019)
❸ Aeolian sand drift surface
❓ Missing core sample with WWL basal contact
Ⓑ
Cross-set thickness (m)
Rs= 0.61
p-value = 0.005
Rs= 0.07
p-value = 0.058
Cross-sets thickness > 50 cm
Ⓒ
FC thickness (m)
Rs= 0.71
p-value = 0.049
nth occurrence (from bottom to top)
Ⓓ
WWL thickness (m)
Rs= -0.36
p-value = 0.117
nth occurrence (from bottom to top)

Figure 15